Fine Tuning of the Photoacoustic Generation Efficiency by Aggregation-Caused Quenching and Excitation Energy Transfer in Bodipy-Labeled Polylactide Nanoparticles

Jean-Baptiste Bodin[1,2], Clément Linger[2,3], Jérôme Gateau[3], Théo Beguin[1], Théotim Lucas[3,4], Laurence Moine[2], David Chapron[2], Minh-Huong Ha-Thi[1], Anam Fatima[1], Gilles Clavier[5], Nicolas Tsapis[2]*, Rachel Méallet[1]*

[1] Université Paris-Saclay, CNRS, Institut des Sciences Moléculaires d'Orsay, 91405 Orsay, France.

[2] Université Paris-Saclay, CNRS, Institut Galien Paris-Saclay, 91400 Orsay, France.

[3] Sorbonne Université, CNRS, INSERM, Laboratoire d'Imagerie Biomédicale, LIB, 75006 Paris, France

[4] Université Paris Cité, CNRS, Matière et Systèmes Complexes, MSC, 75006 Paris, France.

[5] Université Paris-Saclay, ENS Paris-Saclay, CNRS, PPSM, 91190 Gif-sur-Yvette, France.

E-mail: rachel.meallet-renault@universite-paris-saclay.fr

nicolas.tsapis@universite-paris-saclay.fr

Keywords: Photoacoustic, Nanoparticles, Bodipy, Aggregation-caused-quenching, Energy Transfer

Abstract

The relationship between the fluorescence decrease by Aggregation-Caused Quenching (ACQ) and the Photoacoustic Generation Efficiency in polylactide-Bodipy nanoparticles (PLA-Bodipy NPs) is demonstrated. PLA NPs with different PLA-Bodipy loading (from 2.5% to 50% by weight) were studied using a calibrated photoacoustic spectrophotometer. We demonstrate the presence of two photoacoustic emission regimes thanks to the determination of the Global PhotoAcoustic Efficiency (GPAE) which represents the averaged Photoacoustic Generation Efficiency (PGE) over the whole studied band (680-870 nm). In the monomer regime, below 10% by weight of PLA-Bodipy, the fluorescence emission from the Bodipy monomer limits the GPAE. Above 10% of PLA-Bodipy, in the ACQ regime, non-radiative deactivations from the aggregates are predominant and GPAE reaches a high value of 93%. We also introduce the photoacoustic brightness B_{PA}, as the produce of the GPAE by the molar extinction coefficient of NPs. When Bodipy is aggregated, high nanoparticular extinction coefficients (2.4×10^8 L.mol^{-1}.cm^{-1} for **NP-50%**) and high GPAE values are reached leading to ultrabright NPs (22×10^7 L.mol^{-1}.cm^{-1}). Finally, we show that high laser fluences (1-3.5 mJ.cm^{-2}) can significantly reduce the photoacoustic signal by ground state depopulation at the band maximum excitation (-20% for **NP-2.5%**). This non-linear effect can be highly reduced with NPs in the ACQ regime. Above 10% PLA-Bodipy, NPs exhibit intense photoacoustic brightness and low signal loss by nonlinear effects. A

mathematical fit of the absorption and photoacoustic excitation spectra allowed to introduce the Band PhotoAcoustic Efficiency (BPAE) to spectrally differentiate the averaged photoacoustic efficiency at the band maximum $BPAE_{red}$ and in the vibrational shoulder $BPAE_{blue}$. The $BPAE_{red}$ highly depends on the laser fluence due to high ground state depopulation, whereas the $BPAE_{blue}$ does not change with the fluence thanks to a lower laser fluence saturation.

Introduction

In medicine, nanoparticles (NPs) are promising to treat pathologies like cancer, autoimmune and inflammatory diseases, diabetes and neurodegenerative diseases[1] and recently to reduce the SARS-CoV-2 pandemic (from 2020)[2]. However, despite significant development of active and passive targeting, the actual proportion of NPs reaching the diseased tissue remains low[3]. To address this limitation, the concept of nanotheranostics has emerged[1]. The idea is to quantify the accumulation of therapeutic NPs by an imaging modality before deciding whether to treat or not the patient with these NPs. To this purpose, the development of clinically transposable NPs co-encapsulating a therapeutic agent and an imaging agent is needed[1,4]. Among imaging modalities, fluorescence imaging in the near infrared region is promising as several fluorescent dyes have been developed and tested *in vivo* in animal models. *In vivo* florescence imaging beyond microscopic depth can be achieved in two dimensions for clinical applications, in particular for intraoperative imaging[5], and in three dimensions using tomographic imaging for preclinical investigations[6]. The image reconstruction is challenging[7] and spatial resolution and location accuracy of fluorescent targets (millimeters) remain weak due to the strong scattering of biological tissues. However, the molecular imaging capabilities of fluorescence technic are a strong asset, especially when combined to highly luminescent NPs. Dye-loaded luminescent polymer NPs are excellent candidates for theranostic applications as they exhibit good biocompatibility and biodegradability (based on polylactide, chitosan, collagen, poly(lactide-co-glycolide),…), they can be functionalized on the surface, they are stable in biological media, and a controlled drug release can obtained[8,9]. Recently, the development of prodrug polymer nanoparticles, with a covalent grafting of the dye or drug to the polymer, allowed to highly increase the loading (up to more than 30% in weight) and reduce burst release problems[10–12].

Usually, a high dye loading is required for easier detection of polymer NPs in fluorescence imaging, but such loading leads to fluorescence loss, detrimental to detection. Indeed at high loading, dyes with planar backbones and aromatic rings are likely to create intermolecular π-π interactions and other interactions like excimer, exciplex, energy hetero-transfer or charge transfers and excited states reactions[13–16]. All these interactions are often referred as Aggregation-Caused Quenching (ACQ) or self-quenching. Additionally, high dye loading in NPs is also likely to favor homo-Excitation Energy Transfer (EET, or exciton diffusion): due to the dyes' close proximity inside the polymer matrix, the energy can be transferred between several emitters before finally being quenched by non-fluorescent aggregates or a trap[17–20]. Thus, if luminescent imaging is still a powerful tool, new imaging technics exploiting the high loading of organic chromophores in NPs would be advantageous to improve the NP detectability and additionally the image spatial resolution. Photoacoustic imaging, which benefits from the non-radiative energy transfer subsequent to light absorption by the dye, shall be one of them.

Photoacoustic imaging is a cost-effective biomedical imaging modality that combines optical excitation and ultrasound detection. This hybrid modality benefits from a high contrast and a great spatial resolution (submillimeter at centimeter depth)[21]. Absorbing molecules are excited by a pulsed nanosecond excitation, then de-excitation through vibrations and collisions with the solvent, or surrounding matrix, create a local heating of the media that subsequently generates an initial pressure increase and an ultrasound wave. In the literature, high non-radiative rate constant k_{nr}, low fluorescent quantum yield Φ_F and a low inter-system crossing rate constant k_{cis}, are often considered to increase the photoacoustic signal [30–33]. Thus, different strategies are used to quench the fluorescence signal and favor non-radiative decays such as quencher encapsulation[22], photoinduced electron transfer[23,24], intramolecular charge transfer[25–28], molecular rotors[29–31], and long backbone spacers to conserve intramolecular motion in the solid state[29,30,32–34]. Therefore, the fluorescence loss with high dye-loaded polymer NPs is a very promising strategy to favor non-radiative decays and enhance the photoacoustic signal. If some papers mentioned the ACQ effect in dye-loaded NPs to improve the photoacoustic signal[23,35,36], it is rarely seen as a real strategy for photoacoustic enhancement and, to the best of our knowledge, no proper quantification of the photoacoustic efficiency increase in relation with the fluorescence loss has been performed so far.

Herein, we investigate the relationship between the photophysical properties of the dye-loaded polymer NPs and the generated photoacoustic signal for different dye loadings and various excitation fluences. Our objective is to unravel mechanisms that enhance the efficiency of the energy conversion between light absorption and ultrasound emission. The initial pressure increase p_0 in a solution of absorbing NPs illuminated at the excitation wavelength λ and with a the laser fluence $I(\lambda)$ in mJ.cm^{-2}, can be written as[37]:

$$p_0(\lambda) = PGE(\lambda, I(\lambda), H) \cdot \Gamma \cdot \ln(10) \cdot \varepsilon(\lambda, H) \cdot C_{NP} \cdot I(\lambda) \quad (1)$$

where $PGE(\lambda, I(\lambda), H)$ is the Photoacoustic Generation Efficiency, Γ is the Grüneisen coefficient of the solvent, C_{NP} is the NP concentration in mol.L^{-1}, ε is the molar absorptivity of NP in L.mol^{-1}.cm^{-1} at the excitation wavelength. H represents the NP dye loading and can be expressed as the mass percentage of the dye in a NP. $\ln(10)$ is the natural logarithm of 10. $\ln(10) \cdot \varepsilon(\lambda, H) \cdot C_{NP} \cdot I(\lambda)$ is the absorbed optical energy per unit of volume of the NP solution. Part of this energy is converted into heat, with the photothermal conversion efficiency. Then, the conversion of the heat energy to the initial pressure rise p_0 is described by the Grüneisen coefficient of the solution. For diluted sample of polymer NPs, the Grüneisen coefficient of the solution equals that of the solvent. Finally, PGE is a dimensionless parameter which represents the efficiency of conversion of given wavelength absorbed light energy into heat, and subsequently into acoustic energy for the NP suspension. The PGE is the produce of the

photothermal conversion efficiency and the ratio of Grüneisen coefficients between the solution and the solvent. A PGE of 1.0 corresponds to a sample solution for which the absorbed optical energy is fully converted into pressure in a medium with the Grüneisen coefficient of the solvent. PGE may vary with the excitation wavelength λ[37]. Because of the dye aggregation, the PGE and the molar absorptivity ε can be a function of *H*. Moreover, non-linear phenomena may result in a variation of PGE with laser fluence $I(\lambda)$[38]. For clinical applications, it is important to limit the fluence to avoid tissues damage[39]. Moreover, the nanoparticle concentration should also be restrained to avoid toxicity concerns[40]. Thus, two main parameters can be tuned to enhance the photoacoustic signal: the PGE and the molar absorptivity. Both parameters can be strongly enhanced thanks to high dye loading in polymer NPs.

To this attempt, we exploit a calibrated photoacoustic spectrophotometer[37] and a robust Bodipy-loaded polylactide NP recent formulation[40]. Absorption, steady-state and time resolved emission, as well as calibrated photoacoustic spectra (at an incident fluence around 0.98 mJ.cm^{-2}) were studied on PLA-Bodipy NPs with different PLA-Bodipy loadings: from 2.5% to 50% by weight. We define and introduce a new photoacoustic parameter: the Global PhotoAcoustic Efficiency (GPAE), which represents the weighted average of the PGE over the whole studied band (680-870 nm). By studying the GPAE and the non-radiative rate constant of the Bodipy NPs, we demonstrate the presence of two photoacoustic emission regimes: a monomer regime and an ACQ regime. We propose a mathematical model to predict the minimum dye loading for polymer NP to reach the ACQ regime, simply by exploiting the absorption and emission spectra, the molar absorptivity and the Strickler-Berg relation[41].

The high performance of the NPs for photoacoustic imaging were highlighted by the calculation of the NP photoacoustic brightness $B_{PA.}$ B_{PA} was defined as the produce of the maximum molar extinction coefficient of NPs (ε_{NP}) by the GPAE.

Finally, we demonstrate the loss of photoacoustic signal at high laser fluence (3.5 mJ.cm^{-2}) at the band maximum by ground state depopulation. This non-linear effect is detrimental for photoacoustic imaging and can be suppressed with NPs in the ACQ regime. Above 10% of PLA-Bodipy, NPs exhibit high PGE, high photoacoustic brightness, and poor signal loss by nonlinear effect.

Methods

Materials

DL-lactide was purchased from Biovalley, Polysciences Inc. (USA). Poly(ethylene glycol) methyl ether (OH-PEG-OCH_3, average M_n = 5000 $g.mol^{-1}$) was obtained from Iris Biotech GmbH (Germany). Anhydrous toluene, stannous 2-ethyl hexanoate (stannous octoate, $Sn(Oct)_2$), sodium cholate, tetrahydrofuran (THF) spectroscopic grade and all the reagents for the Bodipy synthesis were purchased from Sigma-Aldrich (France) or TCI (France) and used as received. Spectroscopic experiments were conducted in spectroscopic grade dichloromethane (DCM) from Sigma-Aldrich (France). Milli-Q water was used (Reference system Merck-Millipore, France).

Bodipy and polymer synthesis : See Supplementary Information.

Nanoparticles synthesis : See Supplementary Information.

Nanoparticle characterization

NP hydrodynamic diameter (Dynamic light scattering (DLS)), zeta potential and polydispersity index (PDI) were determined with a Zetasizer Nano ZS (Malvern, France) at 25°C, with a 632.8 nm laser (backscatter angle of 173°). The Bodipy encapsulation efficiencies were evaluated as described in 40 thanks to a calibration curve (Beer-Lambert's law) of PLA-Bodipy absorption at 757 nm in DCM as a function of the concentration (slope: $\varepsilon_{PLA\text{-}Bodipy}$ = 78 000 $L.mol^{-1}.cm^{-1}$, DCM, 757 nm). The mean Bodipy number per NP ($N_{PLA\text{-}Bodipy}$) was determined in 40 by computing the ratio of the experimental Bodipy concentration C_{Bodipy} to the nanoparticle concentration C_{NP} (determined by Nanoparticle Tracking Analysis[40]). The nanoparticle molar extinction coefficient was evaluated in 40 thanks to $\varepsilon_{NP} = N_{PLA-Bodipy} \times \varepsilon_{PLA-Bodipy}$.

The Bodipy distance to the nearest neighbor <R> (nm) was determined thanks to:

$$< R > \; = 0.554 \times \frac{1}{n_{PLA-Bodipy}^{1/3}}$$

with $n_{PLA\text{-}Bodipy}$ the number of Bodipy per particle per nm^3 [42]. Differential Scanning Calorimetry experiments were performed on Bodipy NP (50 $mg.mL^{-1}$ of polymer in water) with a VP-DSC microcalorimeter (Perkin-Elmer DSC Diamond), 1°C per min, from 5°C to 70°C, three repeated scans.

Theoretical fluence saturation

The theoretical fluence saturation of the Bodipy dye at 680 nm and 757 nm, was calculated thanks to $F_{saturation}^{\lambda} = \frac{1}{0.38\times10^{-20}\times\varepsilon_{PLA-Bodipy}(\lambda)} . \frac{hc}{\lambda}$ [39], *h* the Planck constant, *c* the speed of light in vacuum ($m.s^{-}$

[1]), λ the wavelength of the laser (m), and $\varepsilon_{PLA\text{-}Bodipy}$ the PLA-Bodipy extinction coefficient (L.mol^{-1}.cm^{-1}) and F the saturation fluence (J.cm^{-2}). $\varepsilon_{PLA\text{-}Bodipy}$ (757 nm) = 80 000 L.mol^{-1}.cm^{-1} and $\varepsilon_{PLA\text{-}Bodipy}$ (680 nm) = 33 200 L.mol^{-1}.cm^{-1}. By definition, at $F_{laser} = F_{saturation}$, 37% of the initial absorbance signal is lost. The theoretical fluence saturation is 0.86 mJ.cm^{-2} at 757 nm and 2.3 mJ.cm^{-2} at 680 nm.

Bodipy reprecipitation experiments : See Supplementary Information.

Photophysical measurements

Spectra were obtained in 10 mm path length quartz cuvettes. For UV-visible spectra a Shimadzu UV-visible spectrophotometer UV-2600 was used. Fluorescence emission spectra were recorded on a Fluoromax-4 spectrofluorimeter (Jobin-Yvon; Horiba). Signals were corrected from the instrument response and from the lamp fluctuations. The absorption was checked to be lower than 0.1 to avoid inner filter effects and fluorescence signals were normalized to account for the absorbance at the excitation wavelength $I_{corr} = \frac{I}{1-10^{-A}}$. The nanoparticles' fluorescence quantum yield (QY) was determined using the **Bodipy** in DCM at 25°C as a reference and $\frac{\Phi_F^x}{\Phi_F^0} = \frac{1-10^{-A_0}}{1-10^{-A_x}} \frac{S_x}{S_0} \left(\frac{n_x}{n_0}\right)^2$ where the index and exponent 0 and x correspond to the reference and the Bodipy NP, respectively, Φ_F is the fluorescence quantum yield, A is the absorbance at the excitation wavelength 670 nm (or 540 nm), S is the integral of the emission curve and n the refractive index. n_x = 1.4242 corresponds to DCM at 25°C and n_0 = 1.33 to water at 25°C. Φ_F^0 = 0.007 was determined in 40.

Time-resolved fluorescence was measured with the Horiba Scientific NanoLED-785L (950 V, 781 nm, <200 ps), the deltaHub™ controller and the DeltaDiode™ controller (Jobin-Yvon; Horiba), in a 10 mm path length quartz cuvette on the Fluoromax-4 (Jobin-Yvon; Horiba). The emission was collected at 820 nm and a preset peak of 12 000 counts. The lamp signal was collected with a colloidal silica solution 40% by weight (Ludox® HS-40) from Sigma Aldrich to scatter the excitation light. All fluorescence decays were fitted using the Levenberg–Marquardt algorithm and a non-linear least-squares fit. The fitted functions were either a bi-exponential function $y = A + B_1 e^{-\frac{t}{T_1}} + B_2 e^{-\frac{t}{T_2}}$ or a sum of a monoexponential and a Kohlrausch function (stretched exponential) $y = A + B_1 e^{\left(-\frac{t}{T_1}\right)^{\beta}} + B_2 e^{-\frac{t}{T_2}}$ [43]. Fit quality was estimated thanks to the variance of weight residuals χ^2. Good fit quality was estimated with $\chi^2 < 1.2$. The average lifetime was estimated for a bi-exponential fit $\overline{\tau} = \frac{B_1 T_1^2 + B_2 T_2^2}{B_1 T_1 + B_2 T_2}$ with B_i the pre-exponential factors and T_i the associated lifetimes. The contribution of each species (species 1 and species 2 associated with T_1 and T_2 respectively) was estimated thanks to $\%1 = \frac{B_1 T_1}{B_1 T_1 + B_2 T_2}$ (relative amplitude). For the Kohlrausch function, the distribution function, H(k), was determined thanks to the inverse Laplace transformation and described in detail in supplementary information.

The radiative rate constant k_r was evaluated using the Strickler-Berg equation[44], $k_r = 2.88 \times 10^{-9} n^2 \frac{\int F(\bar{\nu}_F) d\bar{\nu}_F}{\int \bar{\nu}_F^{-3} F(\bar{\nu}_F) d\bar{\nu}_F} \int \frac{\varepsilon(\bar{\nu}_A) d\bar{\nu}_A}{\bar{\nu}_A}$. The non-radiative rate constant was estimated from $\overline{\tau}$ and k_r values: $k_{nr} = \frac{1}{\overline{\tau}} - k_r$. The Bodipy NPs' Förster radii R_0 were calculated as described in 45 with an orientation factor of 0.476 (for molecules randomly oriented in a rigid matrix)[44], water refractive index of 1.33, and the molecular Bodipy extinction coefficient (80 000 $L.mol^{-1}.cm^{-1}$ at 757 nm). The Bodipy NPs' QY in absence of acceptor was supposed to be the **NP-2.5%** QY (0,009), as for **NP-2.5%** the Bodipy is the most dispersed in the polymer matrix.

Solvatochromism: See Supplementary Information.

Transient absorption spectroscopy: See Supplementary Information.

Photoacoustic spectrum measurements

Photoacoustic excitation spectra (PES) in spectroscopic units were obtained on a home-built calibrated photoacoustic spectrometer[46]. The setup is composed of a tunable nanosecond laser to excite the sample (680-970 nm, pulse width <8ns, pulse repetition rate: 20Hz, SpitLight 600 OPO, Innolas, Germany). PES between 680 and 970 nm were obtained with 10 nm steps. Ultrasound (US) detection was performed with an US linear array (L7-4, ATL, USA) driven by a programmable US machine (Vantage, Verasonics, USA) used in receive-only mode. Samples (15µL) were injected in PTFE tubes (inner diameter: 0.2 mm, Bola, Germany) using 33-gauge needles and a 50µL glass syringe (Hamilton). Tubes were placed at 2.5 cm from the detector surface and perpendicular to the imaging plane. For acoustic coupling, the tubes and the US detector were immersed in a thermostatic water bath filled with ultrapure water (Purelab Option Q, ELGA LabWater). The temperature of the bath was maintained at 25°C (Optima T100-ST12, Grant) for the stability of thermodynamic parameters implied in the photoacoustic process such as the speed of sound and the Grüneisen coefficient. Excitation light was guided in a fiber bundle with two outputs arranged in lines, placed on each side of the US detector, immersed in water, and oriented toward the imaging plane. The illumination surface was evaluated in air to be rectangular with a width of 1 cm along the direction of the tube and a length of 5.5 cm. With this illumination surface and the total energy at the fiber outputs (Pyroelectric Energy sensor ES245C, Thorlabs), the fluence at the location of the tube was evaluated to have a maximum value of 3.5 $mJ.cm^{-2}$ at 760 nm. With polarizing optics between the output of the laser and the input of the fiber bundle, the fluence at 760 nm was varied between 3.5 $mJ.cm^{-2}$ and 0.3 $mJ.cm^{-2}$, by steps of 0.63 $mJ.cm^{-2}$. This fluence does not account for the light propagation in water (about 3 cm from the fiber output to the tubes) which is expected to reduce the angular divergence of light and the light energy due to absorption. Moreover, the laser energy was not constant over the whole spectral range and had a maximum around 730 nm (figure S1). For each fluence, the PA spectrometer was calibrated with a

solution of $CuSO_4$, $5H_2O$ at a concentration of 0.25M. Following this calibration, samples were injected successively. For each laser fluence, five Bodipy NPs were studied: **NP-2.5%**, **NP-5%**, **NP-10%**, **NP-25%** and **NP-50%**. **NP-50%** were diluted three times and **NP-25%** were diluted 2 times, no dilution was performed for **NP-2.5%**, **NP-5%** and **NP-10%**. We verified that no detectable absorption remained in the tubes between two samples by systematically measuring a background reference (ultrapure water). The PES were computed in spectroscopic units (photoacoustic absorbance: PAbs). For the calibration, a dimensionless PGE of 1.107, independent of the excitation wavelength, was used for the solution of $CuSO_4$, $5H_2O$ to account for the Grüneisen coefficient of this reference solution compared to water. A dimensionless PGE equal to 1.0 corresponds to a sample for which the absorbed optical energy is fully converted into pressure in a medium with the Grüneisen coefficient of the water. With the calibration, PAbs corresponds to the product of the PGE and the optical absorption that would be determined for an optical length of 1 cm. PAbs is unitless and can be directly compared with the absorption measurements performed with a spectrophotometer in a 10 mm path length cuvette.

The samples were injected twice in four tubes (three times for the lowest fluence 0.35 $mJ.cm^{-2}$). For each tube, a spectrum was obtained by averaging ultrasound data over 15 laser pulses (30 laser pulses for the lowest fluence). For each laser fluence, a total of 8 spectra (12 for the lowest fluence) were obtained per sample. The median values and the Median Absolute Deviation (MAD) $MAD = 1.4826 \cdot median(|PAbs_i - median(PAbs_i)|)$ were computed. To check that the photoacoustic signal variations with the laser fluence do not arise from experimental artifacts, photoacoustic excitation spectra of a nigrosin (CAS 8005-03-6, Sigma-Aldrich) solution (water, C = $4.84x10^{-4}$ or $9.51x10^{-4}$ $mol.L^{-1}$) were determined at 25°C with the same laser fluences used for Bodipy NPs and compared to the absorption spectra.

Photoacoustic spectrum analysis: GPAE and global photoacoustic brightness

For the solution of NPs, the dimensionless PGE was defined at a given excitation wavelength λ as: $PGE(\lambda) = \frac{PAbs(\lambda)}{A(\lambda)}$ where A is the absorbance of the solution. This PGE corresponds to a spectral photoacoustic efficiency. To obtain a scalar parameter for the investigated spectral range, we define the GPAE. GPAE is the weighted continuous average value of the spectral photoacoustic efficiency on the interval [λ_1 = 680 nm, λ_2 = 870nm] with weight equal to the optical absorption. The formula for the GPAE is : $GPAE = \frac{\int_{\lambda_1}^{\lambda_2} A(\lambda) \cdot PGE(\lambda)\, d\lambda}{\int_{\lambda_1}^{\lambda_2} A(\lambda)\, d\lambda} = \frac{\int_{\lambda_1}^{\lambda_2} PAbs\,(\lambda) d\lambda}{\int_{\lambda_1}^{\lambda_2} A\,(\lambda) d\lambda}$. The GPAE corresponds to an averaged PGE that accounts for the contribution of each wavelength in the whole band. The integrals were calculated on the experimental spectral range thanks to the Origin software (OriginLab) and the trapezoidal rule. The

GPAE was calculated, for each NP batch, from photoacoustic excitation spectrum measured with a low fluence (0.98 mJ.cm^{-2}), to avoid non-linear effects.

By comparison with the fluorescence brightness, we defined a global photoacoustic brightness B_{PA}: $B_{PA} = N_{PLA-Bodipy} \cdot \max_{[\lambda_1;\lambda_2]}(\varepsilon_{PLA-Bodipy}(\lambda_1)) \cdot GPAE = \max_{[\lambda_1;\lambda_2]}(\varepsilon_{NP}(\lambda)) \cdot GPAE$, with $N_{PLA-Bodipy}$ the number of PLA-Bodipy per NP, $\varepsilon_{PLA-Bodipy}$ the polymer extinction coefficient (mol.L^{-1}.cm^{-1}) and ε_{NP} the NP extinction coefficient. The maximum value of the extinction coefficient over the investigated spectral range was taken. NP photoacoustic brightness was calculated, for each NP batch, from GPAE value calculated with a low laser fluence (0.98 mJ.cm^{-2}), to avoid non-linear effects.

PES and UV-spectra fitting

Gaussian peak fitting was found to adequately model the spectral shape of the absorption spectrum of indocyanine green (ICG)[47]. As for ICG modeled by a sum of two Gaussian functions, the absorption spectrum of Bodipy comprises a dominant band (at 760 nm) and a vibronic shoulder (680-700 nm). Therefore, we implemented a decomposition of the absorption and PA spectra into Gaussian functions. We used a fitting algorithm based on a nonlinear least-squares solver (trust-region-reflective method) to determine the amplitude a_i, the central wavelength λ_i and the Gaussian Root Mean Square (RMS) width ω_i of each Gaussian function of the sum. $S(\lambda) = \sum_i a_i \exp(-\frac{(\lambda-\lambda_i)^2}{2\omega_i^2})$. We found that for the spectral range covered by the PA spectra, the spectra could be fitted by the sum of two Gaussian functions centered around λ_{red} ≈760 nm (called red Gaussian function) and λ_{blue} ≈ 680 nm (called blue Gaussian function). However, as the PES starts at 680 nm, the Gaussian fitting leads to a large variability for the blue Gaussian function. Therefore, we first implemented the Gaussian peak fitting on the UV-Visible absorption spectra and then used some parameters to fit the different PA spectra.

The absorption spectra were acquired in a broader wavelength range (400 nm – 900 nm) than the PES. However, the absorption did not decrease to almost zero around 610 nm but increased again to a third band centered at 540 nm. We chose to restrict the wavelength range from 530 to 870 nm to add a third Gaussian function (called grey Gaussian function) centered around λ_{grey} ≈ 540 nm. The parameters λ^A_{grey} and ω^A_{grey} of this grey Gaussian function as well as λ^A_{blue} and ω^A_{rblue} of the blue Gaussian were found consistent for **NP-10%**, **NP-25%** and **NP-50%** (about 0.1-0.5% relative standard deviation). For **NP-2.5%** and **NP-5%**, the scattering was no longer negligible, resulting in a wider fitted band for the grey Gaussian function within turns induced some variation on λ^A_{blue}. To avoid this effect, we chose to set the parameters λ^A_{blue} and ω^A_{blue} to the median value over the NP with three highest concentrations in Bodipy (i.e. 10, 25 and 50%): $\lambda^A_{blue,fixed}$ = 685.05 nm and $\omega^A_{blue,fixed}$ = 37.04 nm . Then, we performed again a Gaussian band fitting but with two Gaussian functions only (blue Gaussian at 685.05 nm and

red Gaussian around 760 nm) and in the range 670 nm - 870 nm, to determine the parameters a^{A}_{red}, λ^{A}_{red}, ω^{A}_{red} and a^{A}_{blue} for each nanoparticle.

As the absorption spectra, the PES were fitted with the sum of two Gaussian functions (blue Gaussian at 685.05 nm and red Gaussian around 760 nm). For the blue Gaussian function $\lambda^{A}_{blue,fixed}$ and $\omega^{A}_{blue,fixed}$ were used. As the wavelength step of the PA spectra was loose (every 10 nm), we found that λ^{A}_{red} could be imported from the absorption spectra for each nanoparticle without altering the quality of the fit. This solution facilitated the comparison between the two spectral modalities.

The optimization algorithm could not directly use the uncertainty of the measurements. Therefore, we chose to feed the optimization algorithm not with the median value but with all the spectra to determine a^{PA}_{red}, ω^{PA}_{red} and a^{PA}_{blue} for each NP.

By exploiting the fitted curves, Band PhotoAcoustic Efficiencies (BPAE) could be defined as:

$$BPAE_i = \frac{\int_{\lambda_1}^{\lambda_2} a_i^{PA} \exp\left(-\frac{\left(\lambda-\lambda^{A}{}_i\right)^2}{2(\omega_i^{PA})^2}\right) d\lambda}{\int_{\lambda_1}^{\lambda_2} a_i^{A} \exp\left(-\frac{\left(\lambda-\lambda^{A}{}_i\right)^2}{2(\omega_i^{A})^2}\right) d\lambda}$$

, with i = blue or red. For each band, the BPAE is the ratio of the integrated Gaussian function for photoacoustics to the integrated blue Gaussian function for absorption. $BPAE_{blue}$ and $BPAE_{red}$ are the weighted continuous average PGE of the vibronic shoulder and of the red band, respectively. $BPAE_{blue}$ and $BPAE_{red}$ were calculated for each NP and each laser fluence, respectively.

Results & Discussion

NP formulation

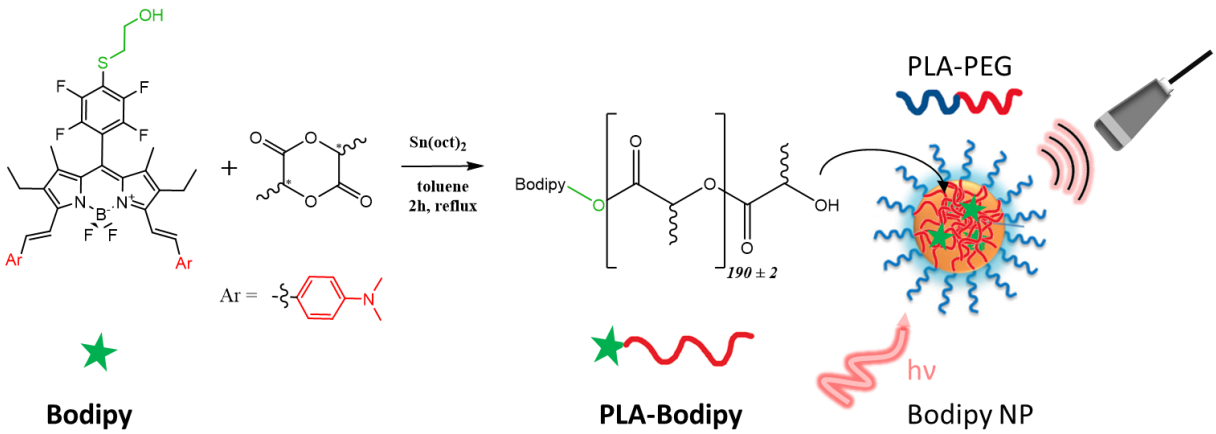

Figure 1. Molecular structure of the Bodipy and PLA-Bodipy and schematic representation of the photoacoustic activated Bodipy NP.

Bodipy was synthesized with the three-steps one pot protocol described in details in 40. As already demonstrated previously, the introduction of two electron-donating groups: 4-(N,N-dimethylamino)styryl, shifts the maximum of absorption close to the Near Infra-Red region (757 nm) and introduces an Internal Charge Transfer (ICT) that quenches the Bodipy fluorescence (QY = 0.007 in dichloromethane). **Bodipy** exhibits strong absorption properties ε (757 nm) = 80 000 $L.mol^{-1}.cm^{-1}$ in dichloromethane and its low fluorescence favors high Photoacoustic signal. Ring Opening Polymerization (ROP) of DL-lactide was initiated by the Bodipy alcohol function to obtain a **PLA-Bodipy** (14 500 $g.mol^{-1}$) (figure 1). PEGylated Bodipy NPs were formulated by emulsion–evaporation technique by mixing different mass percentage of **PLA-Bodipy** (from 2.5% to 50%) compared to $PLA\text{-}PEG_{5000}$: **NP-2.5%**, **NP-5%**, **NP-10%**, **NP-25%** and **NP-50%**. The synthesized NP are monodisperse with a diameter around 100 nm[40].

Photoacoustic response at a fluence of 0.98 $mJ.cm^{-2}$

The PES and absorption spectra of Bodipy NPs are presented in figure 2 and figure S2. For the solutions of Bodipy NPs that were very absorbent and very diluted, we can consider the Grüneisen coefficient of the solution equal to that of the solvent $\Gamma_{sample} \sim \Gamma_{water}$. Therefore, the PGE is inferior or equal to 1 and PAbs represents the part of optical absorption that is effectively transformed into the acoustic

emission. Absorption spectra and PES for **NP-2.5%** and **NP-50%** have very close spectral shapes. The maximum of absorption is around 760 nm and the vibronic shoulder at 680 nm. Comparable results are observed for all the batches (**NP-2.5%**, **NP-5%**, **NP-10%**, **NP-25%**, **NP-50%** figure S2). A slight red shift is observed on the absorption spectra and PES as the PLA-Bodipy amount increases. For **NP-2.5%** we can observe, at any excitation wavelength, a lower PAbs compared to absorption. The PGE, ratio between the photoacoustic absorption and the absorption, is about 74% at 760,4 nm (table 1). The PGE_{760nm} increases when PLA-Bodipy increases. For instance, a PGE_{760nm} of 91% is observed for **NP-50%**. Thus, PES and absorption spectra are getting closer with higher PLA-Bodipy amount. The GPAE was defined as the weighted continuous average value of the PGE on the interval [680 nm, 870nm] with weight equal to the optical absorption, and it was computed as the ratio of the areas under the curve between the PES and the optical absorption over the whole studied spectral range. It represents the overall photoacoustic efficiency of the sample. A GPAE equal to 100% would correspond to a PGE equal to 1 over the entire spectral range and a perfect match between the PES and the absorption spectra. **NP-2.5%** exhibits a 69.3% GPAE and GPAE is increasing up to 92.8% as PLA-Bodipy increases to 50%. **NP-10%**, **NP-25%** and **NP-50%** all display GPAEs higher than 85%. Thus, GPAE seems to increase a lot between 2.5% and 5% of PLA-Bodipy, and changes only slightly above 10% of PLA-Bodipy. It appears that the GPAE is correlated with percentage of PLA-Bodipy in NPs.

The GPAE estimation would usually be based on $(1-\Phi_F)$[48] with Φ_F the fluorescence quantum yield of the particles. The direct determination of the GPAE is more accurate because it only considers non-radiative effects that contribute to the acoustic wave generation. With $(1-\Phi_F)$ estimation, all non-fluorescent phenomena, even those that do not contribute to the thermoelastic expansion, are considered in the calculation. Moreover, the photoacoustic signal not only depends on the GPAE, but also on NP absorption coefficient. Higher PLA-Bodipy per NP will favor higher photoacoustic signal because of a greater absorption. For this reason, **NP-50%** exhibit a much higher PAbs (8.66 at 760 nm) than **NP-25%** (PAbs = 4.55 at 760 nm) (figure S2), even though their respective GPAE are very similar. By comparison with the fluorescence brightness, we define a photoacoustic brightness, $B_{PA}(\lambda)$, product of the NP extinction coefficient and the GPAE. NP brightness are indicated in table S1 as a function of PLA-Bodipy content. The brightest NPs are obtained with **NP-50%**, B_{PA} = 2.2x10^8 L.mol^{-1}.cm^{-1}. For **NP-5%**, **NP-10%** and **NP-25%**, the photoacoustic brightness is 1.2x10^7 L.mol^{-1}.cm^{-1}, 2.5x10^7 L.mol^{-1}.cm^{-1} and 7.9x10^7 L.mol^{-1}.cm^{-1} respectively. To the best of our knowledge, this is the first report of a quantitative determination of the photoacoustic brightness, thanks to a precise determination of the NP GPAE. By comparison with fluorescence imaging, ultrabright Bodipy polymer NPs exhibit fluorescence brightness of 1.4x10^8 L.mol^{-1}.cm^{-1}[49] and dye-loaded polymer NPs have fluorescence brightness about 10^6-10^7 L.mol^{-1}.cm^{-1} [62, 70, 71]. Herein, we have synthesized NPs with high NP extinction coefficient (10^7-10^8 L.mol^{-}

^{1}.cm^{-1} [40]) and very high GPAE that makes them ultrabright photoacoustic emitters. The photoacoustic brightness could be used as a quantitative photophysical parameter to compare *in vitro* different photoacoustic contrast agents.

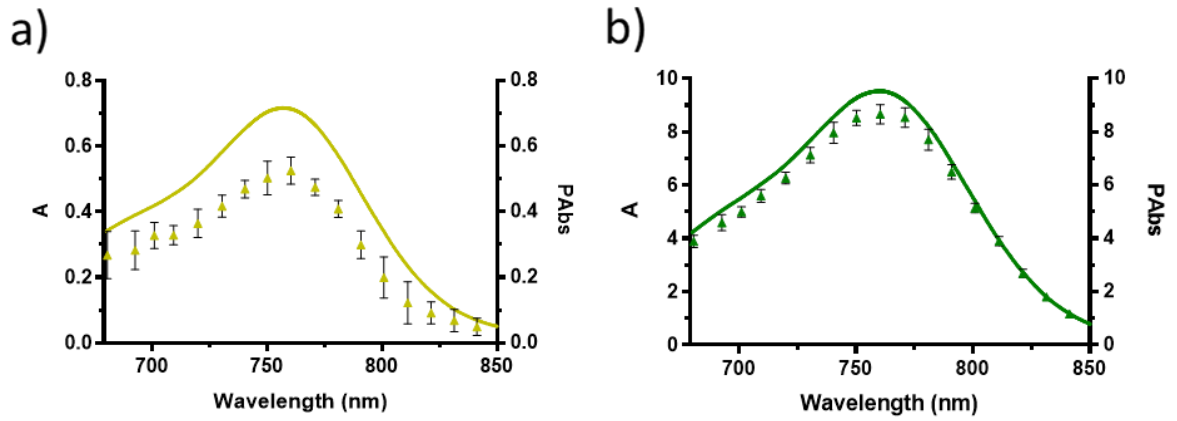

Figure 2. Absorption spectra (continuous line) and PES (triangle) for nanoparticles batch. (a) NP-2.5% (yellow), (b) NP-50% (green). Laser fluence 0.98 mJ.cm^{-2}. The error bars for the PES corresponds to the median value ± MAD. Absorbance values were corrected from dilution factor: no dilution for NP-2.5% and 10 times dilution for NP-50%. PAbs values were corrected from dilution factor: no dilution for NP-2.5% and three times dilution for NP-50%.

	NP-2.5%	NP-5%	NP-10%	NP-25%	NP-50%
GPAE (%)	69.3	80.4	84.8	88.3	92.8
PGE $_{760\ nm}$ (%)	74	79	84	88	91

Table 1: GPAE and PGE$_{760\ nm}$ for each NP batch. GPAE was obtained by computing the area ratio of PES and absorption spectra for each NP batch (680-870 nm).

Characterization of the fluorescence properties

As fluorescence would decrease the PGE since it is a competitive deactivation pathway, we investigated the fluorescence properties of the Bodipy NPs and their relationship with GPAE. First, the QY decrease with the NP dye loading will be discussed. Then, with solvatochromism experiments, we will try to decipher if the fluorescence loss comes from an ACQ effect or from a polymer matrix effect. The presence of J-aggregated Bodipy will be studied thanks to fluorescence excitation spectra, the exciton theory and reprecipitation experiments. Finally, Förster Resonance Energy Transfer (FRET) between the Bodipy in the polymer matrix and different ways of fluorescence quenching will be discussed. Figure 3a presents the NP fluorescence emission spectra, from **NP-2.5%** to **NP-50%**, with a 670 nm excitation. A fluorescence intensity decrease is observed as PLA-Bodipy amount increases. The highest fluorescence signal is obtained for **NP-2.5%** and the lowest for **NP-50%**. The maximum band

position is red-shifted as PLA-Bodipy content increases. NP fluorescence QY relative to the **Bodipy** QY (Φ_F/Φ_F^0) was calculated (figure 3b and table S2). The NP QY is decreasing as PLA-Bodipy percentage increases. **NP-2.5%** have a 125% relative QY**,** when **NP-50%** have a 12% relative QY. We observed a 113 percent loss of the QY. As **Bodipy** is a charge transfer Bodipy, matrix effect may influence the QY and the spectral shift[44]. On the other hand, high dye-loaded polymer NPs are well known to enhance fluorescence ACQ and red-shift behavior[49–52].

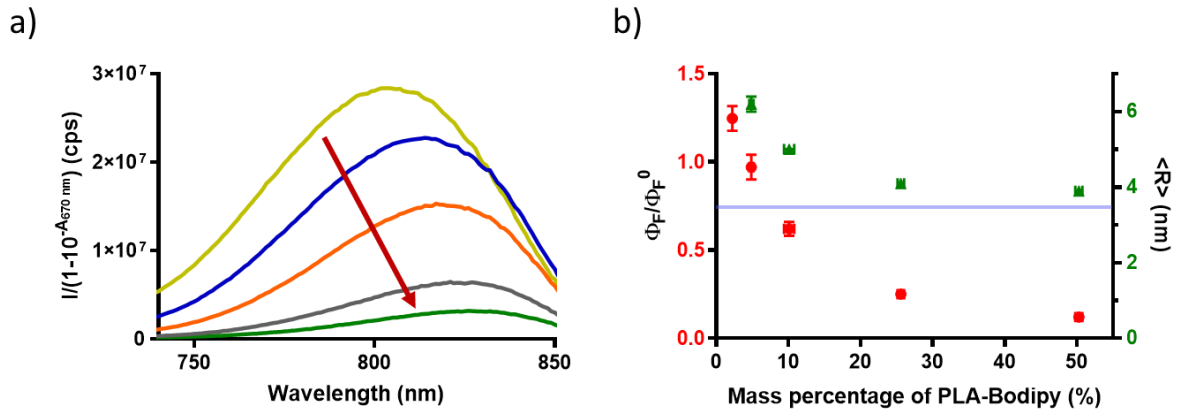

Figure 3. (a) Emission spectra of the NPs (λ_{ex} = 670 nm, slit width 10 nm and A < 0.1). (Yellow, Bodipy NP-2.5%), (blue, Bodipy NP-5%), (orange, Bodipy NP-10%), (grey, Bodipy NP-25%), (green, Bodipy NP-50%). (b) Relative fluorescence quantum yield (red circle) evolution as a function of the PLA-Bodipy mass percentage, excitation at 670 nm. Fluorescence quantum yield (Φ_F) relative to Bodipy, 298 K (Φ_F^0 = 0.007). <R>: average distance of the nearest neighbor between Bodipys (green triangles) evolution as a function of PLA-Bodipy mass percentage. The blue line represents R_0 (nm), the Förster Radius for Bodipy NPs.

To discriminate between ACQ and matrix effect, solvatochromism was studied (figure S3, table S3). For absorption, emission, and excitation spectra of **Bodipy**, a bathochromic shift was observed as solvent polarity increases. The Stokes shift is increasing with the solvent polarity ($E_T(30)$ polarity scale[53]), from 499 cm^{-1} for cyclohexane to 1294 cm^{-1} for methanol. A positive solvatochromism is noticeable, highlighting a higher excited state dipolar moment compared to ground state for **Bodipy**[44]. The charge transfer nature of the electronic transition, from the donor aniline group to the acceptor Bodipy main core, can explain the higher excited state dipole moment. Similar results were obtained in the literature with a close Bodipy structure, and the charge transfer nature of the transition was demonstrated by electron density calculations[54]. For non-polar solvents (cyclohexane, dioxane, toluene, chloroform) a locally excited emission band was noticeable at low wavelength (700 nm). This

emission arises from the Franck-Condon state. At higher wavelength, the solvatochromic main band corresponds to a Twist Intramolecular Charge Transfer state where the dimethylamino group may have twisted 90° compared to the aromatic ring[55,56]. For the different solvents, no change of the fluorescence spectra was observed with the excitation wavelength. In hydrophobic solvent the **Bodipy** QY was improved, QY = 0.16 in cyclohexane. In polar solvent the Bodipy intramolecular charge transfer is favored, and the fluorescence was reduced (QY = 0.009 in methanol). The quenching effect caused by charge transfer was demonstrated in 54, with a close Bodipy structure, and an increased fluorescence when the charge transfer is avoided with a protonated amino group. The increased QY in non-polar solvent can explain the slightly higher QY value for **NP-2.5%** compared to the **Bodipy** in DCM (Φ_F/Φ_F^0 = 125%). In **NP-2.5%**, the Bodipy monomer resides in a hydrophobic and rigid polymer matrix, as DSC shows that polymer glass-transition temperature (T_g) in the NP is 30-33°C, which favors fluorescence more than in DCM. For NPs, no trace of a LE state was observed at low wavelength. Moreover, NP red-shifted emission and absorption are less marked than what was observed in the solvatochromic experiments. Therefore, NP fluorescence loss might arise from ACQ effect rather than from matrix effect.

To investigate the possible presence of several emitters, excitation was changed. Fluorescence emission spectra with a 540 nm excitation were measured (figure S4). The molecular **Bodipy** emission fluorescence spectra (figure S4b) in DCM are unchanged whatever the excitation wavelength (670 or 540 nm). However, for the NP batches, the fluorescence spectral shape is changing upon excitation wavelength change (figure S4a, table S4). Spectral deformations are magnified with high PLA-Bodipy amount. The higher PLA-Bodipy percentage, the weaker the blue shoulder (793 nm; -39% from **NP-2.5%** to **NP-50%**) and the higher the red shoulder (840 nm; +49% from **NP-2.5%** to **NP-50%**) (figure S4d emission). On the contrary, no spectral change with the excitation wavelength was observed in the solvatochromic experiments. This is a good clue to highlight the presence of ACQ in Bodipy NPs. NP relative QY measured with a 540 nm excitation is also decreasing (table S2), but values are slightly different from those obtained with a 670 nm excitation. For all NP batches, the fluorescence emission bands with a 540 nm excitation are thinner than those with a 670 nm excitation (table S4). The Full Width at Half Maximum (FWHM) is sharpening with an increased PLA-Bodipy loading from 927 cm^{-1} to 786 cm^{-1} for the emission with a 540 nm excitation. The same sharpening of the band is observed with the emission spectra with a 670 nm excitation (from 1187 cm^{-1} to 907 cm^{-1}). Excitation spectra of the Bodipy NP show an increased red shoulder (815 nm; +29% from **NP-2.5%** to **NP-50%**) with the PLA-Bodipy amount, but no change in the blue shoulder (700 nm) was observed (figure S4c and S4d).

Change of the fluorescence emission spectra with the excitation wavelength for Bodipy NPs and not for **Bodipy** in DCM, is characteristic of the apparition of a new species inside NPs. The increased

spectral deformation with the PLA-Bodipy content is a strong indication for the appearance of aggregated Bodipy inside NPs. Bodipy aggregation can be explained with the exciton theory and two models of aggregates: sandwich like H-aggregates and head-to-tail or head-head J-aggregates[18,57–59]. The red shoulder increase (emission and excitation spectra) and the red-shift observed in absorption and emission spectra with an increased PLA-Bodipy amount, could arise from red emitters formation: J-aggregates[60–62]. Moreover, a sharp emission band of about 641 cm^{-1} for Bodipy J-aggregates and about 1061 cm^{-1} for Bodipy monomer can be found in the literature[18]. The sharpening of NP emission spectra is a further proof of J-aggregates formation. The blue shoulder decrease in the NP fluorescence emission spectra highlights the disappearance of fluorescent Bodipy, which may be attributed to the non-aggregated Bodipy monomer. On the **Bodipy** structure, alkyl chains on the alpha and beta positions of the Bodipy core are known to induce a twisted pentafluorophenyl (meso position) out of the Bodipy plane by steric hindrance. Similar Bodipy structure in literature show dihedral angle between the indacene plane and the phenyl ring between 55°-88° [54,61,63–65]. The bulky and perpendicular pentafluorophenyl ring can favor J-aggregation compared to H-aggregation thanks to lower intermolecular π-π interactions by steric hindrance[61,65–67]. No clues for the formation of non-fluorescent H-aggregates inside the NP were observed on the NP spectra (absorption blue shift, broadening band in absorption). The QY decrease could come either from dark species formation: EET down to a trap (J-aggregates could act as traps, or bimolecular singlet-singlet annihilation), the presence of less fluorescent J-aggregates, or formation of poorly fluorescent aggregates with intermolecular charge transfer[18,62].

To better decipher the aggregation behavior, **Bodipy** reprecipitation was studied in different water/THF mixtures (figure S5-S7), with THF acting as a good solvent and water as a bad solvent. A red shifted absorption and emission are noticeable when the water fraction increases. First, we observe a decrease of the fluorescence emission as water fraction increases. Moreover, at high water fraction, very similar spectral distortions (blue and red shoulder) as the one of Bodipy NP can be seen. For fluorescence emission (540 nm excitation), a +48% red shoulder (840 nm) increase, and a -41% blue shoulder (793 nm) decrease are visible between 0% and 70% water (figure S6). Those band ratio variations are really close to those obtained within Bodipy NPs. Water/THF excitation spectra (figure S7) highlight a huge increase of the red ratio at 815 nm (+150%) as water fraction increases. Red shift in absorption and emission as well as the red shoulder increases are good clues for J-aggregates formation at high water fraction. The blue shoulder decrease in emission might arise from monomer transformation into aggregated species. The nanoprecipitation experiments, with an increased water fraction, were in good agreement with the observed fluorescence evolution of NPs with an increased PLA-Bodipy amount. As already stated above : the fluorescence loss with an increase water fraction

could come from energy migration to a trap, the presence of less fluorescent J-aggregates, monomer to less fluorescent J-aggregates energy transfer, or intermolecular charge transfer state[18,62].

For Bodipy NPs, distances to the nearest neighbor <R> (figure 3b) were estimated as described in 42 thanks to the mean Bodipy number per NP per nm^3 ($n_{PLA\text{-}Bodipy}$) calculated in details in 40. <R> is decreasing from 6.2 nm for **NP-5%** down to 3.9 nm for **NP-50%** but the values are probably overestimated, as the NP volumes were calculated using NP hydrodynamic diameters. As a matter of fact, Bodipy hydrophobicity is likely to favor aggregation in NP core and not in the hydrophilic polyethylene glycol shell[49,68]. In literature, some J-aggregated Bodipy with a π-π distance of 0.4-1.7 nm are reported[61,65,69–71]. Those values are close to the over-estimated nearest neighbor.

<R> Bodipy values (6-4 nm). The Bodipy mean distance is reducing with the Bodipy loading, as does the NP QY (figure 3b). Spatially close Bodipy in NPs could favor self-energy transfer as well as aggregation. The Förster radius (R_0) was calculated for the Bodipy NPs and indicated table S2 and on figure 3b (blue band). <R> values are close to NP Förster radius 3.4 nm and demonstrates the possible existence of energy transfer inside Bodipy NPs. The energy transfer can be of two different natures: excitation migration, through FRET between several identical emitters (such as J-aggregates or monomers) also known as homo-FRET, or energy transfer between different emitters (hetero-FRET e.g. Monomer to J-aggregates). The very high fluorescence quenching inside Bodipy NPs could either come from hetero-FRET from monomer to less-fluorescent aggregates, or homo-FRET and energy migration down to a trap (dark species or bimolecular singlet-singlet annihilation) or both. Such behavior is consistent with literature, dye loaded polymeric nanoparticles are known to exhibit multi-steps energy transfers between aggregates (homo-FRET or exciton diffusion)[17,51,72,73].

Link between the GPAE and the fluorescence properties of the NPs

We have demonstrated that an increased dye loading is likely to favor J-aggregated Bodipy formation in NPs and fluorescence quenching. Time-resolved experiments were performed to better decipher deactivation pathways and how they can be connected to acoustic wave generation (figure 4a). The fluorescence lifetime of Bodipy NPs is decreasing as PLA-Bodipy content increases. The fastest fluorescence deactivation is observed with **NP-50%** and the longest one with **NP-2.5%**. Mean fluorescence lifetimes ($\bar{\tau}$) were estimated thanks to a bi-exponential fit (Table S5). The mean lifetime decreased from 1.22 ns for **NP-2.5%** down to 0.27 ns for **NP-50%**. The excited state lifetime is decreasing as PLA-Bodipy increases, as for the QY values, suggesting a stable radiative rate constant (k_r) and favored non radiative decays. The radiative rate constant k_r was calculated with the Strickler-

Berg relation[41] (table S5). We observe the same value for all NP batches ($k_r \approx 1.4x10^8$ s^{-1}). The non-radiative rate constant k_{nr} was estimated and is linearly increasing with PLA-Bodipy amount (figure 4b, table S5). Excited state lifetime and QY decrease arise from favored non-radiative decay with as PLA-Bodipy content increases and highlight ACQ effect in NPs. The y-intercept of the fit, $k_{nr}^0 = 7.4\times10^8$ s^{-1} (1.1 ns equivalent lifetime), corresponds to a limit situation: isolated Bodipy monomer inside a polylactide matrix. The 1.1 ns lifetime, is close to the one of **Bodipy** in DCM (1.03 ns)[40]. Similar k_{nr} linear increase was obtained on Bodipy-loaded polymer NPs in literature[49]. The mathematical fit highlights two terms dependency for k_{nr}: a constant non-radiative deactivation of the Bodipy monomer (y-intercept $k_{nr}^0 = 7.4\times10^8$ s^{-1}) and the aggregation caused quenching term, which depends on the PLA-Bodipy percentage: $k_{ACQ} = 7.08 \times 10^7 \times \%PLA - Bodipy$. The overall equation obtained is: $k_{nr} = k_{nr}^0 + k_{ACQ}$, and a similar equation was noticeable in literature[74]. According to the mathematical fit equation, above the calculated value of 10.5% PLA-Bodipy, k_{ACQ} starts to be higher than k_{nr}^0 and aggregation caused quenching becomes the favored non-radiative deactivation pathway. For PLA-Bodipy below **NP-10%**, the favored deactivation pathway is the Bodipy monomer non-radiative decay (monomer regime). For dye loading above **NP-10%**, the favored deactivation is operated by ACQ (ACQ regime).

GPAE was plotted as a function of k_{nr} (figure 4c). GPAE highly depends on the Bodipy aggregation state, it is increasing very fast with k_{nr} for low PLA-Bodipy NP: **NP-2.5%** and **NP-5%**. Above 10% PLA-Bodipy (GPAE = 84.8%), in the ACQ regime, the GPAE increase is slower and further aggregation will poorly change its value. The fit of k_{nr} as a function of the PLA-Bodipy percentage might be used as a highly predictive tool to estimate the minimal PLA-Bodipy content to be in the ACQ regime. From the fluorescence lifetime measurement, one can therefore predict the minimum PLA-Bodipy content to quickly reach high GPAE.

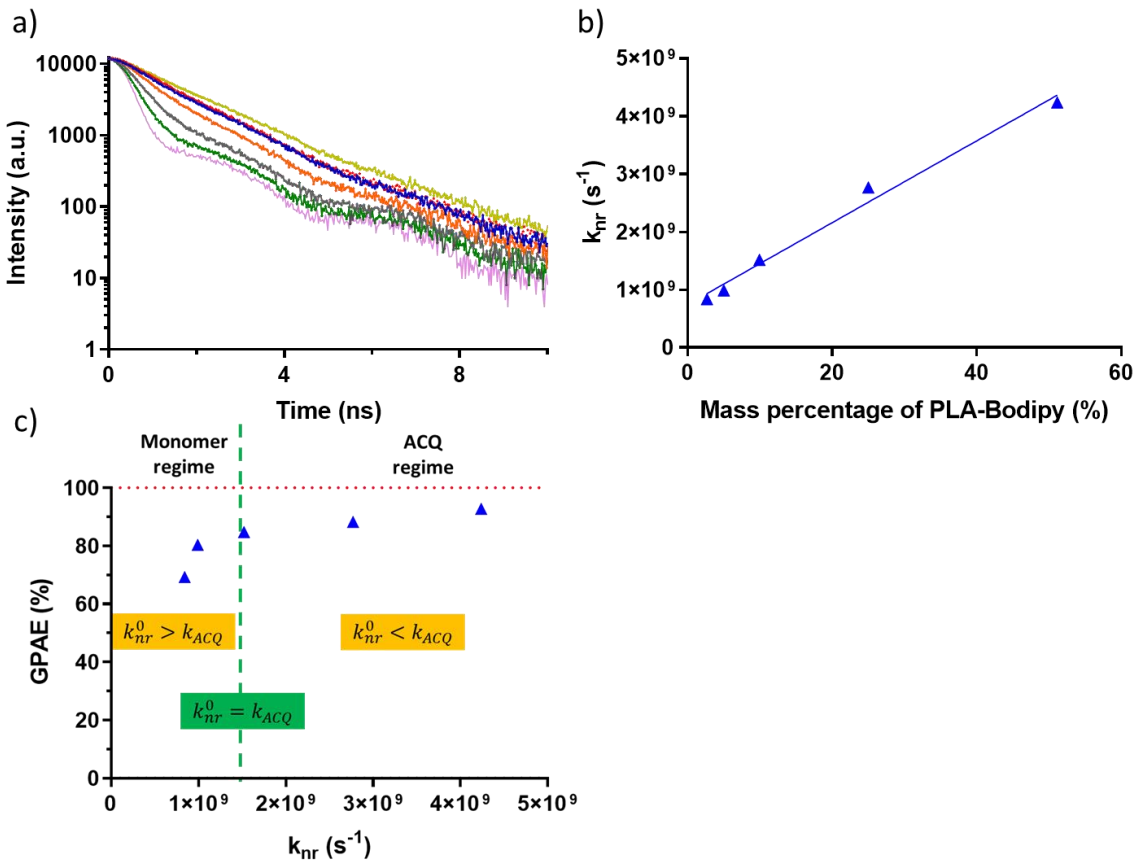

Figure 4. (a) Fluorescence decays of NP solution, excitation at 781 nm with a pulsed diode <200 ps, emission at 820 nm. (Yellow, Bodipy NP-2.5%), (Red, Bodipy in DCM), (blue, Bodipy NP-5%), (orange, Bodipy NP-10%), (grey, Bodipy NP-25%), (green, Bodipy NP-50%), (purple, excitation diode signal). (b) Evolution of the non-radiative rate constant k_{nr} as a function of the introduced mass percentage of PLA-Bodipy. The rate constants were determined thanks to the Strickler-Berg equation. Absorbance linear fit: R^2 = 0.9869 and $y = 7.08 \times 10^7 x + 7.44 \times 10^8$. (c) Evolution of the GPAE as a function of the non-radiative rate constant. The red line represents the curve $\mathbf{GPAE} = \mathbf{100}\%$.

Heterogeneity of the Bodipy aggregates was evaluated by fitting the fluorescence decays with a sum of a mono-exponential function (Bodipy monomer, T_2) and a stretched exponential function (lifetime distribution of the aggregates, T_1)[43,49]. The fitted parameters and the curves are indicated figure S9 and S10, and the mono-exponential lifetime was fixed at T_2 = 1.1 ns (**Bodipy** lifetime in DCM). Results show a decrease in the aggregates lifetime (T_1) from 0.5 ns (**NP-5%**) to 0.1 ns (**NP-50%**) with increasing the PLA-Bodipy percentage. The aggregates lifetime is decreasing due to favored non-radiative decay thanks to ACQ. Aggregates relative amplitude (%1) is increasing with the PLA-Bodipy percentage: from 16.3% (**NP-5%**) to 94.8% (**NP-50%**). We can notice that above 10% of PLA-Bodipy, a relative amplitude

of the Bodipy aggregates higher than 50% was obtained (68.4%). As seen before, above 10% PLA-Bodipy, the aggregation caused quenching is the favored deactivation pathway (ACQ regime). The beta exponent is decreasing as PLA-Bodipy content increases and highlights an increased inhomogeneity in the NP[49]. The distribution of aggregates lifetime, H(k), is plotted figure S11a. We can observe a broadening of lifetime distribution as PLA-Bodipy content increases that is characteristic of the increased inhomogeneity in Bodipy interactions. The aggregates rate (%1), obtained with the fitted parameter for stretched exponential, is plotted as a function of the PLA-Bodipy percentage and stacked with the Bodipy NP relative QY curve (figure S11b). The aggregate contribution is increasing (+79%) as the Bodipy QY is decreasing (-88%). Fluorescence quenching is then indeed related with the aggregate concentration in the polymer matrix.

So far and to summarize we have demonstrated that the fluorescence quenching by ACQ and excitation energy transfer could highly favor non-radiative deactivation and therefore increase the GPAE up to 93%. Above 10% of PLA-Bodipy, the ACQ regime is reached with GPAE greater than 90%. Higher PLA-Bodipy percentage than **NP-10%** will poorly improve the GPAE.

PGE in different absorption bands and for different incident laser fluences

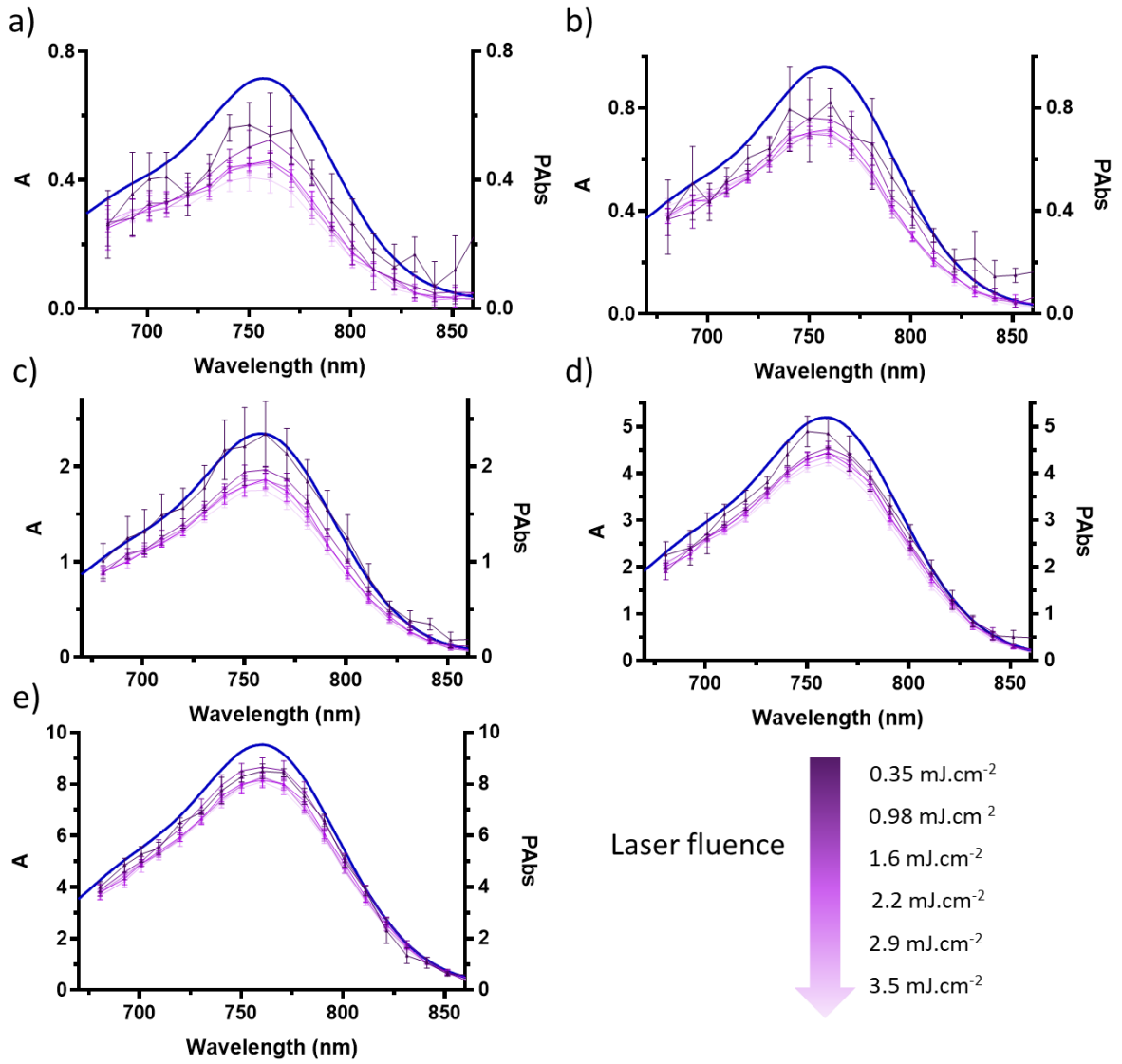

Figure 5: Absorption spectra (continuous line) and PES (dots) of Bodipy NP for different laser fluences. (a) NP-2.5%, (b) NP-5%, (c) NP-10%, (d) NP-25%, (e) NP-50%. From dark to light violet respectively 0.35 mJ.cm^{-2}, 0.98 mJ.cm^{-2} and 1.6 mJ.cm^{-2}, 2.2 mJ.cm^{-2}, 2.9 mJ.cm^{-2}, 3.5 mJ.cm^{-2}. The arrow indicates the laser fluence increase. The error bars for the PES corresponds to the median value ± MAD.

The Photoacoustic efficiency was studied over the whole absorption band and characterized with the GPAE. However, one can notice some spectral differences of the PGE. In the blue region, between 680-700 nm, PAbs and Absorbance are very close, even for NPs with low GPAE as **NP-2.5%** and **NP-5%** (figure 2 and S1). However, the proximity of PES and absorption spectra is lowered at the band maximum. To better visualized the spectral variability, absorption spectra and photoacoustic excitation spectra were superimposed and normalized at 680.6 nm for each NP batch and the fluence

was increased up to 3.5 mJ.cm^{-2} (figure S12). For low PLA-Bodipy loading, **NP-2.5%** and **NP-5%,** in PES, the maximum of the band is closer to the vibronic shoulder than in absorption spectra. It seems that the maximum band shrivel up for low PLA-Bodipy loading PES. For **NP-25%** and **NP-50%**, a perfect match was observed between normalized absorption and PES. In the literature, this band deformation for photoacoustic spectra compared to absorption spectra was also observed with bis-styryl Bodipy, but never commented nor explained[75,76]. It was also noticeable in literature on fluorescent proteins[77]. The spectral deformation of the band might arise from non-linear effects caused by high fluence irradiation on the sample. To verify this hypothesis, five different laser fluences were used, 0.35 mJ.cm^{-2}, 0.98 mJ.cm^{-2} and 1.6 mJ.cm^{-2}, 2.2 mJ.cm^{-2}, 2.9 mJ.cm^{-2}, 3.5 mJ.cm^{-2} and photoacoustic spectra plotted and compared with absorption spectra measured on a classical UV-visible spectrophotometer (with no fluence variation) (figure 5). For each NP batch, the PAbs is reduced as the fluence increases. The PAbs is getting further and further away from the absorption spectra with an increased fluence, a signature of lower energy conversion between absorbed light and acoustic emission. One can notice that the influence of the laser fluence is higher on low PLA-Bodipy loaded NPs (**NP-2.5%**, **NP-5%** and **NP-10%**) than on high PLA-Bodipy loaded NPs: **NP-50%** and **NP-25%.** Moreover, as seen before on the PES spectra (figure S2 and S12), spectral differences are also visible. For each NP batch, the PAbs loss as fluence increase, is higher at the maximum band than in the vibronic shoulder (680-700 nm). Very few PAbs variations with the fluence were observed between 680 and 700 nm for all NP batches. To finely characterized and quantify the photoacoustic signal loss, the GPAE was calculated for each NP batch and each laser fluence and plotted figure 6 (a). For each NP batch, an increased fluence leads to lower GPAE. This loss of efficiency is the consequence of the PAbs decrease with laser fluence at the maximum band (figure 6). GPAE is rather stable for **NP-50%,** GPAE = 92% at 0.35 mJ.cm^{-2} and 86% at 3.5 mJ.cm^{-2}, close to the calculated **NP-50%** GPAE (93%, figure 2). By contrast, low PLA-Bodipy loaded NPs exhibit even lower GPAE as fluence increases: 18% decrease for **NP-2.5%**, from 79% at 0.35 mJ.cm^{-2} to 61% at 3.5 mJ.cm^{-2}. Aggregation can highly reduce the influence of the laser fluence on the GPAE. The same irradiations fluences were also evaluated on a nigrosin aqueous solution (figure S13). No change of the nigrosin spectra is observed with the laser fluence confirming that PAbs decrease arises from nonlinear effects in Bodipy NPs and not from experimental artefacts.

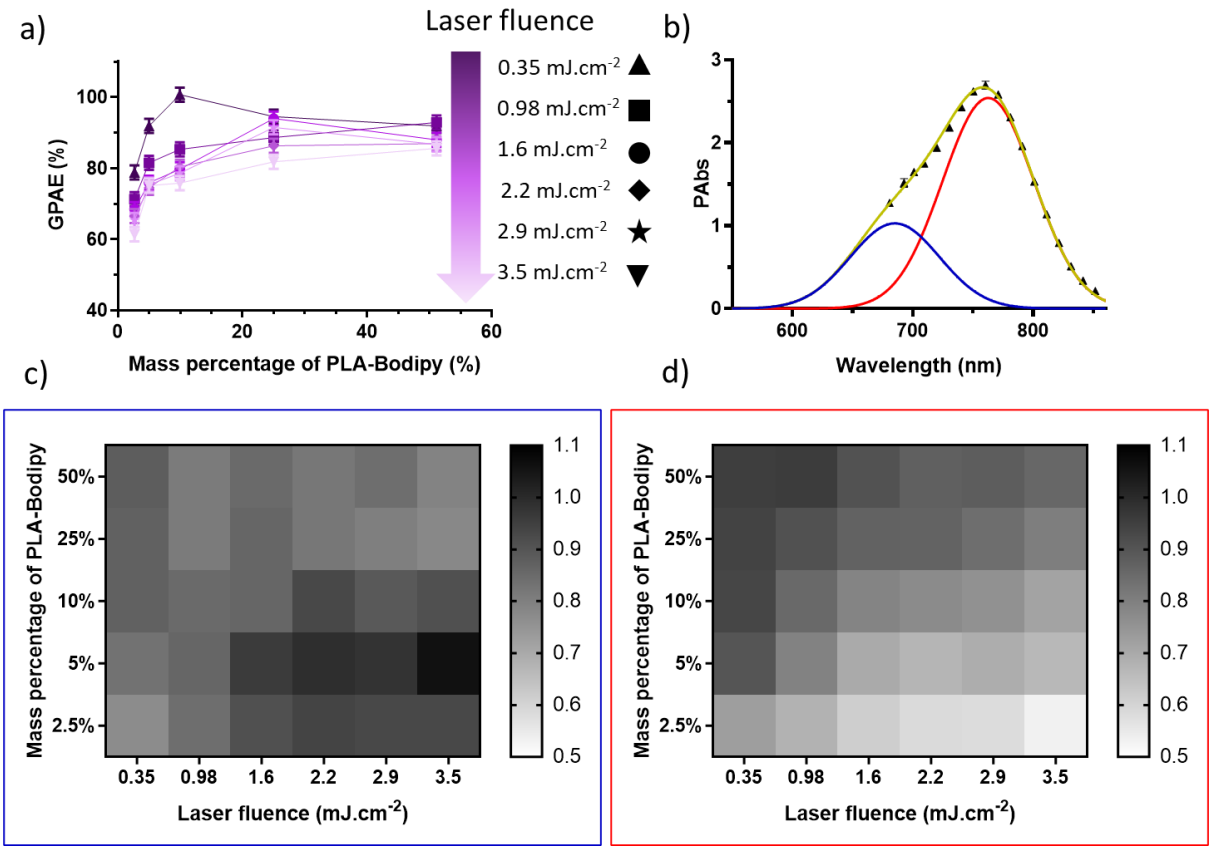

Figure 6. (a) GPAE as a function of mass percentage of PLA-Bodipy. From dark to light violet respectively 0.35 mJ.cm^{-2} (triangles), 0.98 mJ.cm^{-2} (squares), 1.6 mJ.cm^{-2} (circles), 2.2 mJ.cm^{-2} (rhombus), 2.9 mJ.cm^{-2} (stars), 3.5 mJ.cm^{-2} (upside down triangle). The arrow indicates the laser fluence increase. (b) Photoacoustic excitation spectra of NP-50% with a 3.5 mJ.cm^{-2} laser fluence (dark triangles). Total fit curve (yellow) composed of two Gaussian functions (in red and blue). NP-50% were diluted three times. (c) BPAE$_{blue}$ values displayed with a gray colormap. (d) BPAE$_{red}$ values displayed with a gray colormap.

We were able to evaluate the GPAE. However, due to significant spectral shift between absorption spectra and PES, and fewer experimental points for PES (10 nm steps), we were not able to study PGE spectral dependencies. To evaluate the spectral dependency of the photoacoustic efficiency, PES were fitted with two Gaussian functions, one for the vibronic shoulder at 680 nm (blue curve) and another for the maximum of absorption and the red part (red curve) (730-870 nm) (figure 6 (b)). The same fitting procedure was operated on absorption spectra for each NP batch. The results are indicated in figure 6 (b) and figures S14-S18, for each NP batch and each laser fluence. Fitting allows to differentiate the photoacoustic efficiency from the vibronic shoulder and from the maximum band. Similarly, to the GPAE, Band photoacoustic efficiencies BPAE were defined as the weighted average of the PGE over each band. BPAE$_{blue}$ and BPAE$_{red}$ are plotted as a function of the incident laser fluence and the mass percentage of PLA-Bodipy with gray colormaps (figure 6 (c) and (d)). BPAE$_{blue}$ values are very high,

between 0.8 and 1 for each NP and each fluence and seem to be randomly distributed, with no clear evolution with the laser fluence, nor the PLA-Bodipy loading. For each NP batch, the standard deviation of the $BPAE_{blue}$ values were between 3 to 7%, which is negligible. The blue vibronic shoulder is very efficient for photoacoustic emission and its BPAE does not depends on the laser fluence. By contrast, the red band is highly affected by the laser fluence. For each NP batch, we can observe a decrease of the acoustic efficiency with an increased laser fluence. For **NP-50%** a 9% decrease of $BPAE_{red}$ between 0.35 $mJ.cm^{-2}$ and 3.5 $mJ.cm^{-2}$ laser fluence is observed and for **NP-2.5%** a 20% decrease was measured. As seen before, the photoacoustic signal loss is reduced with NPs containing aggregated Bodipy. The lowest photoacoustic efficiency for the maximum band, $BPAE_{red}$ = 53%, was observed with **NP-2.5%** and 3.5 $mJ.cm^{-2}$ irradiation. The highest $BPAE_{red}$ was measured with **NP-50%** (0.98 $mJ.cm^{-2}$) $BPAE_{red}$ = 96%. To summarize, on the one hand, the vibronic shoulder shows high BPAE and no variation with the laser fluence nor the PLA-Bodipy loading. On the other hand, the maximum band highly depends on laser fluence and PLA-Bodipy loading. High energy non-linear effect seems to only affect the Bodipy maximum band.

Nanosecond-transient absorption of the Bodipy NPs and its link to the non-linear photoacoustic behavior

To better understand the nonlinear effect, ns-transient absorption experiments were conducted. The **Bodipy** nanosecond transient absorption spectra in DCM are plotted in figure S20. Bodipy triplet is not observed, and the excited state goes back to the ground state in about a few tens of nanoseconds. The transient absorption spectra of Bodipy highlights the presence of excited state absorption between 550 and 675 nm, and the ground state photobleaching between 680 and 770 nm accompanied by the emission between 790 nm and 850 nm. In literature, push-pull Bodipys show similar band positions[62,78,79]. Intersystem crossing (k_{CIS}) could have reduced the PA signal[80], but according to transient absorption spectra, Bodipy does not show any triplet spectral and kinetics signatures. PAbs loss by dye degradation (bleaching) are also negligible, as demonstrated in 40 and the absorbance value was checked to remain constant between before and after the experiments. Transient absorption spectra of the NP batches, **NP-5%**, **NP-25%** and **NP-50%** were also recorded (figure S21) and no new bands can be observed. In the nanosecond regime, Bodipy NPs have the same excited state spectra as **Bodipy** in DCM. However, the excited state population is decreasing with the PLA-Bodipy loading. Transient absorption values (absolute value$|\Delta A|$) are lower with high PLA-Bodipy percentage. The lowest $|\Delta A|$ signal is obtained with **NP-50%** and the highest is measured on **Bodipy** in DCM. Those results are in good agreement with Bodipy NP excited state lifetime, which is decreasing as PLA-Bodipy loading increases (table S5, figure S8). Aggregation favors very fast non-radiative deactivations to the ground state. **NP-50%** has a very low excited state absorption, a low ground state

photobleaching and a weak emission in the nanosecond regime. On the contrary, **NP-5%** exhibit great signal for excited state absorption, ground state photobleaching and emission. The short-excited state lifetime of **NP-50%** and **NP-25%** makes them less sensitive to nonlinear effects in the excited state. **NP-2.5%** and **NP-5%,** however, have longer excited state lifetimes (about 1 ns).

As seen on the transient absorption spectra, ground state photobleaching is increasing close to the maximum of absorption. On the photoacoustic setup, for one pulse excitation, with a high fluence and NP with long excited state lifetime, the ground state is so much excited with early incoming photons that there are not enough molecules remaining in the ground state for later incoming photons. This is ground state depopulation (or ground state photobleaching): excited state is saturated, and absorbance values are decreasing with the laser fluence[81]. Lower absorption leads to lower photoacoustic emission, and lower PAbs. On the photoacoustic setup, PAbs is decreasing with the laser fluence, as shown figure 6. NPs containing Bodipy as aggregates, **NP-50%** and **NP-25%,** return very fast to the ground state by non-radiative deactivation, leading to less ground state depletion and lower PAbs and PGE loss. Similar results were observed in literature on other chromophores photoacoustic spectra, but no quantification nor justification of the ground state depletion was proposed[38,77]. On Bodipy NPs, ground state depletion effect is maximum at the maximum of absorption and causes a 20% loss of the $BPAE_{red}$ for **NP-2.5%** between 0.35 $mJ.cm^{-2}$ and 3.5 $mJ.cm^{-2}$. As seen on NP transient absorption spectra, far from the absorption maximum, in the vibronic shoulder, ground state depletion effect is lower, thanks to a lower absorptivity. The laser fluence to reach saturation was calculated for Bodipy as detailed in 39. By definition, at the saturation fluence, 37% of the initial absorbance is lost. The theoretical fluence saturations are 0.86 $mJ.cm^{-2}$ at 760 nm and 2.3 $mJ.cm^{-2}$ at 680 nm. In the vibronic shoulder, around 680 nm, almost all the irradiation energies tested were lower than fluence saturation one (2.3 $mJ.cm^{-2}$): ground state depopulation was not observed and the $BPAE_{blue}$ remains constant. On the contrary, at the band maximum, more irradiation energies were higher than the saturation fluence (0.86 $mJ.cm^{-2}$) and caused ground state photobleaching and a $BPAE_{red}$ influenced by laser fluences. Aggregation Caused Quenching is therefore a powerful tool to limit photoacoustic loss by non-linear effects. With **NP-25%** and **NP-50%** very limited PAbs variations and high $BPAE_{red}$ were measured for each laser fluence.

Conclusion

We have studied and quantified the relationship between fluorescence quenching by Aggregation-Caused Quenching and photoacoustic generation efficiency enhancement in PLA-Bodipy NPs. PLA NPs with different PLA-Bodipy loading (from 2.5% to 50% by mass) were studied using a calibrated photoacoustic spectrophotometer. We defined a Global photoacoustic efficiency (GPAE) representing

the weighted average, over the whole band, of the photoacoustic generation efficiency. GPAE is equal to 100% if all the absorbed energy is converted in ultrasound regardless of the excitation wavelength over the whole spectral range. To quantify the high performance of NPs in photoacoustic imaging, we have also defined the photoacoustic brightness B_{PA}, as the produce of the GPAE by the maximum molar extinction coefficient of NPs in the investigated spectral range. Ultrabright NPs (1.2-22 x 10^7 $L.mol^{-1}.cm^{-1}$) are obtained thanks to great photoacoustic efficiency of NPs containing aggregated Bodipy (GPAE = 93% for **NP-50%**) and high molar extinction coefficients (1.5x10^7-2.4x10^8 $L.mol^{-1}.cm^{-1}$). Two regimes for photoacoustic emission exist: a monomer regime and an Aggregation-Caused Quenching regime. In the monomer regime, below 10% by weight of PLA-Bodipy, fluorescence emission from the Bodipy monomer limits the GPAE. Above 10% of PLA-Bodipy, in the ACQ regime, non-radiative deactivations are predominant and the GPAE reaches a high asymptotic value of 93%. Finally, we have shown that at high laser fluences (1-3.5 $mJ.cm^{-2}$), at the maximum of the absorption band, a significant loss of the photoacoustic signal is remarkable by ground state depopulation (-20% for **NP-2.5%**). This non-linear effect can be limited with NPs in the ACQ regime. The use of such NPs (Above 10% PLA-Bodipy) allows to work at high laser fluence without loss of photoacoustic signal. We have developed a fine mathematical fit of the absorption and photoacoustic spectra to calculate an average photoacoustic efficiency at the band maximum $BPAE_{red}$ and in the vibrational shoulder $BPAE_{blue}$. The fit allows us to spectrally differentiate the photoacoustic efficiency in the absorption band and to demonstrate that only the red band is affected by the ground state depopulation.

Author Contributions

JBB, CL, JG, TB, TL, LM, DC, M-HH-T, AF, GC, NT, RM

Conceptualization : GC, JG, NT and RM, Methodology: JBB, GC, JG, LM, NT and RM, Validation: JBB, CL, GC, JG, LM, NT and RM, Formal analysis: JBB, CL,TB, TL and JG, Investigation: JBB, CL, TB, TL, M-HH-T, AF, JG, TL, DC, Writing, JBB, CL, JG, GC, NT and RM, Visualization: JBB, CL, JG, NT and RM, Supervision: JG, GC, NT and RM,

Project Administration: JG, GC, NT and RM, Funding Acquisition: JG, GC, NT, and RM.

Supporting Information.

Materials and methods.

Figure S1. Laser energy

Figure S2. Absorption spectra and photoacoustic excitation spectra

Figure S22: Linearity between PAbs and A

Acknowledgements

We sincerely thank Elise Michel for assistance in the synthesis of Bodipy. This project has received funding by the French National Research Agency under the program ANR-21-CE09-0024-01. RM thanks the Région Ile-de-France and DIM NanoK for financial support as well as CHARMMMAT LabEx. The University Paris-Saclay and the CNRS are acknowledged for funding as well as Région Ile de France for the LAZRX photoacoustic set-up (Sésame).

This work was supported by a grant from the Ministère de l'Education Nationale, de l'Enseignement Supérieur et de la Recherche, Contrat Doctoral Spécifique Normalien, for Jean-Baptiste BODIN's Ph.D. thesis (ED 2MIB N°571). C. Linger PhD fellowship was funded by CNRS (80 Prime).

This project has received financial support from the CNRS through the MITI interdisciplinary programs (Defi Imag'IN).

References

(1) Mura, S.; Couvreur, P. Nanotheranostics for Personalized Medicine. *Adv Drug Deliv Rev* **2012**, *64* (13), 1394–1416. https://doi.org/10.1016/j.addr.2012.06.006.

(2) Tenchov, R.; Bird, R.; Curtze, A. E.; Zhou, Q. Lipid Nanoparticles–From Liposomes to MRNA Vaccine Delivery, a Landscape of Research Diversity and Advancement. *ACS Nano* **2021**, *15* (11), 16982–17015. https://doi.org/10.1021/acsnano.1c04996.

(3) Torrice, M. Does Nanomedicine Have a Delivery Problem? *ACS Cent. Sci.* **2016**, *2* (7), 434–437. https://doi.org/10.1021/acscentsci.6b00190.

(4) Fornaguera, C.; García-Celma, M. J. Personalized Nanomedicine: A Revolution at the Nanoscale. *J Pers Med* **2017**, *7* (4), E12. https://doi.org/10.3390/jpm7040012.

(5) Zhu, B.; Sevick-Muraca, E. M. A Review of Performance of Near-Infrared Fluorescence Imaging Devices Used in Clinical Studies. *BJR* **2015**, *88* (1045), 20140547. https://doi.org/10.1259/bjr.20140547.

(6) Stuker, F.; Ripoll, J.; Rudin, M. Fluorescence Molecular Tomography: Principles and Potential for Pharmaceutical Research. *Pharmaceutics* **2011**, *3* (2), 229–274. https://doi.org/10.3390/pharmaceutics3020229.

(7) Zhang, P.; Ma, C.; Song, F.; Fan, G.; Sun, Y.; Feng, Y.; Ma, X.; Liu, F.; Zhang, G. A Review of Advances in Imaging Methodology in Fluorescence Molecular Tomography. *Phys Med Biol* **2022**, *67* (10). https://doi.org/10.1088/1361-6560/ac5ce7.

(8) Fattal, E.; Hillaireau, H.; Mura, S.; Nicolas, J.; Tsapis, N. Targeted Delivery Using Biodegradable Polymeric Nanoparticles. In *Fundamentals and Applications of Controlled Release Drug Delivery*; Siepmann, J., Siegel, R. A., Rathbone, M. J., Eds.; Advances in Delivery Science and Technology; Springer US: Boston, MA, 2012; pp 255–288. https://doi.org/10.1007/978-1-4614-0881-9_10.

(9) Zielińska, A.; Carreiró, F.; Oliveira, A. M.; Neves, A.; Pires, B.; Venkatesh, D. N.; Durazzo, A.; Lucarini, M.; Eder, P.; Silva, A. M.; Santini, A.; Souto, E. B. Polymeric Nanoparticles: Production, Characterization, Toxicology and Ecotoxicology. *Molecules* **2020**, *25* (16), 3731. https://doi.org/10.3390/molecules25163731.

(10) Delplace, V.; Couvreur, P.; Nicolas, J. Recent Trends in the Design of Anticancer Polymer Prodrug Nanocarriers. *Polym. Chem.* **2014**, *5* (5), 1529–1544. https://doi.org/10.1039/C3PY01384G.

(11) Nicolas, J. Drug-Initiated Synthesis of Polymer Prodrugs: Combining Simplicity and Efficacy in Drug Delivery. *Chem. Mater.* **2016**, *28* (6), 1591–1606. https://doi.org/10.1021/acs.chemmater.5b04281.

(12) Gao, P.; Nicolas, J.; Ha-Duong, T. Supramolecular Organization of Polymer Prodrug Nanoparticles Revealed by Coarse-Grained Simulations. *J. Am. Chem. Soc.* **2021**, *143* (42), 17412–17423. https://doi.org/10.1021/jacs.1c05332.

(13) Huang, Y.; Xing, J.; Gong, Q.; Chen, L.-C.; Liu, G.; Yao, C.; Wang, Z.; Zhang, H.-L.; Chen, Z.; Zhang, Q. Reducing Aggregation Caused Quenching Effect through Co-Assembly of PAH Chromophores and Molecular Barriers. *Nat Commun* **2019**, *10* (1), 169. https://doi.org/10.1038/s41467-018-08092-y.

(14) Leduskrasts, K.; Suna, E. Aggregation Induced Emission by Pyridinium–Pyridinium Interactions. *RSC Adv.* **2018**, *9* (1), 460–465. https://doi.org/10.1039/C8RA08771G.

(15) Liu, Z.; Jiang, Z.; Yan, M.; Wang, X. Recent Progress of BODIPY Dyes With Aggregation-Induced Emission. *Frontiers in Chemistry* **2019**, *7*.

(16) Ein Konzentrationsumschlag Der Fluoreszenz. *Zeitschrift für Physikalische Chemie* **1954**, *1* (5_6), 275–277. https://doi.org/10.1524/zpch.1954.1.5_6.275.

(17) Reisch, A.; Didier, P.; Richert, L.; Oncul, S.; Arntz, Y.; Mély, Y.; Klymchenko, A. S. Collective Fluorescence Switching of Counterion-Assembled Dyes in Polymer Nanoparticles. *Nature Communications* **2014**, *5* (1), 1–9. https://doi.org/10.1038/ncomms5089.

(18) Vu, T. T.; Dvorko, M.; Schmidt, E. Y.; Audibert, J.-F.; Retailleau, P.; Trofimov, B. A.; Pansu, R. B.; Clavier, G.; Méallet-Renault, R. Understanding the Spectroscopic Properties and Aggregation Process of a New Emitting Boron Dipyrromethene (BODIPY). *J. Phys. Chem. C* **2013**, *117* (10), 5373–5385. https://doi.org/10.1021/jp3097555.
(19) Caponetti, V.; Trzcinski, J. W.; Cantelli, A.; Tavano, R.; Papini, E.; Mancin, F.; Montalti, M. Self-Assembled Biocompatible Fluorescent Nanoparticles for Bioimaging. *Frontiers in Chemistry* **2019**, *7*.
(20) Chen, B.; Wang, F. Combating Concentration Quenching in Upconversion Nanoparticles. *Accounts of Chemical Research* **2019**, *53*. https://doi.org/10.1021/acs.accounts.9b00453.
(21) Beard, P. Biomedical Photoacoustic Imaging. *Interface Focus* **2011**, *1* (4), 602–631. https://doi.org/10.1098/rsfs.2011.0028.
(22) Qin, H.; Zhou, T.; Yang, S.; Xing, D. Fluorescence Quenching Nanoprobes Dedicated to In Vivo Photoacoustic Imaging and High-Efficient Tumor Therapy in Deep-Seated Tissue. *Small* **2015**, *11* (22), 2675–2686. https://doi.org/10.1002/smll.201403395.
(23) Lyu, Y.; Fang, Y.; Miao, Q.; Zhen, X.; Ding, D.; Pu, K. Intraparticle Molecular Orbital Engineering of Semiconducting Polymer Nanoparticles as Amplified Theranostics for in Vivo Photoacoustic Imaging and Photothermal Therapy. *ACS Nano* **2016**, *10* (4), 4472–4481. https://doi.org/10.1021/acsnano.6b00168.
(24) Merkes, J. M.; Lammers, T.; Kancherla, R.; Rueping, M.; Kiessling, F.; Banala, S. Tuning Optical Properties of BODIPY Dyes by Pyrrole Conjugation for Photoacoustic Imaging. *Advanced Optical Materials* **2020**, *8* (11), 1902115. https://doi.org/10.1002/adom.201902115.
(25) Qi, J.; Chen, C.; Zhang, X.; Hu, X.; Ji, S.; Kwok, R. T. K.; Lam, J. W. Y.; Ding, D.; Tang, B. Z. Light-Driven Transformable Optical Agent with Adaptive Functions for Boosting Cancer Surgery Outcomes. *Nat Commun* **2018**, *9* (1), 1848. https://doi.org/10.1038/s41467-018-04222-8.
(26) Guo, B.; Sheng, Z.; Hu, D.; Li, A.; Xu, S.; Manghnani, P.; Liu, C.; Guo, L.; Zheng, H.; Liu, B. Molecular Engineering of Conjugated Polymers for Biocompatible Organic Nanoparticles with Highly Efficient Photoacoustic and Photothermal Performance in Cancer Theranostics. *ACS Nano* **2017**, *11*. https://doi.org/10.1021/acsnano.7b04685.
(27) Wang, S.; Li, Z.; Liu, Y.; Feng, G.; Zheng, J.; Yuan, Z.; Zhang, X. Activatable Photoacoustic and Fluorescent Probe of Nitric Oxide for Cellular and in Vivo Imaging. *Sensors and Actuators B: Chemical* **2018**, *267*, 403–411. https://doi.org/10.1016/j.snb.2018.04.052.
(28) Li, X.; Liu, L.; Li, S.; Wan, Y.; Chen, J.-X.; Tian, S.; Huang, Z.; Xiao, Y.-F.; Cui, X.; Xiang, C.; Tan, Q.; Zhang, X.-H.; Guo, W.; Liang, X.-J.; Lee, C.-S. Biodegradable π-Conjugated Oligomer Nanoparticles with High Photothermal Conversion Efficiency for Cancer Theranostics. *ACS Nano* **2019**, *13* (11), 12901–12911. https://doi.org/10.1021/acsnano.9b05383.
(29) Qi, J.; Feng, L.; Zhang, X.; Zhang, H.; Huang, L.; Zhou, Y.; Zhao, Z.; Duan, X.; Xu, F.; Kwok, R. T. K.; Lam, J. W. Y.; Ding, D.; Xue, X.; Tang, B. Z. Facilitation of Molecular Motion to Develop Turn-on Photoacoustic Bioprobe for Detecting Nitric Oxide in Encephalitis. *Nat Commun* **2021**, *12* (1), 960. https://doi.org/10.1038/s41467-021-21208-1.
(30) Zhao, Z.; Chen, C.; Wu, W.; Wang, F.; Du, L.; Zhang, X.; Xiong, Y.; He, X.; Cai, Y.; Kwok, R. T. K.; Lam, J. W. Y.; Gao, X.; Sun, P.; Phillips, D. L.; Ding, D.; Tang, B. Z. Highly Efficient Photothermal Nanoagent Achieved by Harvesting Energy via Excited-State Intramolecular Motion within Nanoparticles. *Nat Commun* **2019**, *10* (1), 768. https://doi.org/10.1038/s41467-019-08722-z.
(31) Cai, X.; Liu, J.; Liew, W. H.; Duan, Y.; Geng, J.; Thakor, N.; Yao, K.; Liao, L.-D.; Liu, B. Organic Molecules with Propeller Structures for Efficient Photoacoustic Imaging and Photothermal Ablation of Cancer Cells. *Mater. Chem. Front.* **2017**, *1* (8), 1556–1562. https://doi.org/10.1039/C7QM00056A.
(32) Liu, S.; Zhou, X.; Zhang, H.; Ou, H.; Jacky, W.; Liu, Y.; Shi, L.; Ding, D.; Tang, B. Moleculer Motion in Aggregates: Manipulating TICT for Boosting Photothermal Theranostics. *Journal of the American Chemical Society* **2019**, *141*. https://doi.org/10.1021/jacs.8b13889.

(33) Diez-Cabanes, V.; Monari, A.; Pastore, M. Competition between the Photothermal Effect and Emission in Potential Phototherapy Agents. *J. Phys. Chem. B* **2021**, *125* (31), 8733–8741. https://doi.org/10.1021/acs.jpcb.1c03977.
(34) Gao, H.; Duan, X.; Jiao, D.; Zeng, Y.; Zheng, X.; Zhang, J.; Ou, H.; Qi, J.; Ding, D. Boosting Photoacoustic Effect via Intramolecular Motions Amplifying Thermal-to-Acoustic Conversion Efficiency for Adaptive Image-Guided Cancer Surgery. *Angewandte Chemie International Edition* **2021**, *60* (38), 21047–21055. https://doi.org/10.1002/anie.202109048.
(35) Zhang, J.; Yang, C.; Zhang, R.; Chen, R.; Zhang, Z.; Zhang, W.; Peng, S.-H.; Chen, X.; Liu, G.; Hsu, C.-S.; Lee, C.-S. Biocompatible D–A Semiconducting Polymer Nanoparticle with Light-Harvesting Unit for Highly Effective Photoacoustic Imaging Guided Photothermal Therapy. *Advanced Functional Materials* **2017**, *27* (13), 1605094. https://doi.org/10.1002/adfm.201605094.
(36) Zhang, J.; Chen, J.; Ren, J.; Guo, W.; Li, X.; Chen, R.; Chelora, J.; Cui, X.; Wan, Y.; Liang, X.-J.; Hao, Y.; Lee, C.-S. Biocompatible Semiconducting Polymer Nanoparticles as Robust Photoacoustic and Photothermal Agents Revealing the Effects of Chemical Structure on High Photothermal Conversion Efficiency. *Biomaterials* **2018**, *181*, 92–102. https://doi.org/10.1016/j.biomaterials.2018.07.042.
(37) Lucas, T.; Sarkar, M.; Atlas, Y.; Linger, C.; Renault, G.; Gazeau, F.; Gateau, J. Calibrated Photoacoustic Spectrometer Based on a Conventional Imaging System for In Vitro Characterization of Contrast Agents. *Sensors* **2022**, *22* (17), 6543. https://doi.org/10.3390/s22176543.
(38) Hatamimoslehabadi, M.; Bellinger, S.; La, J.; Ahmad, E.; Frenette, M.; Yelleswarapu, C.; Rochford, J. Correlation of Photophysical Properties with the Photoacoustic Emission for a Selection of Established Chromophores. *J. Phys. Chem. C* **2017**, *121* (43), 24168–24178. https://doi.org/10.1021/acs.jpcc.7b07598.
(39) Paschotta, D. R. *Saturation Energy*. https://www.rp-photonics.com/saturation_energy.html (accessed 2022-01-24).
(40) Bodin, J.-B.; Gateau, J.; Coïs, J.; Lucas, T.; Lefebvre, F.; Moine, L.; Noiray, M.; Cailleau, C.; Denis, S.; Clavier, G.; Tsapis, N.; Méallet-Renault, R. Biocompatible and Photostable Photoacoustic Contrast Agents as Nanoparticles Based on Bodipy Scaffold and Polylactide Polymers: Synthesis, Formulation, and In Vivo Evaluation. *ACS Appl. Mater. Interfaces* **2022**, *14* (36), 40501–40512. https://doi.org/10.1021/acsami.2c04874.
(41) Strickler, S. J.; Berg, R. A. Relationship between Absorption Intensity and Fluorescence Lifetime of Molecules. *J. Chem. Phys.* **1962**, *37* (4), 814–822. https://doi.org/10.1063/1.1733166.
(42) Santos, M. B. On the Distribution of the Nearest Neighbor. *American Journal of Physics* **1986**, *54* (12), 1139–1141. https://doi.org/10.1119/1.14731.
(43) Berberan-Santos, M. N.; Bodunov, E. N.; Valeur, B. Mathematical Functions for the Analysis of Luminescence Decays with Underlying Distributions 1. Kohlrausch Decay Function (Stretched Exponential). *Chemical Physics* **2005**, *315* (1), 171–182. https://doi.org/10.1016/j.chemphys.2005.04.006.
(44) Valeur, B.; Berberan-Santos, M. N. *Molecular Fluorescence: Principles and Applications*; John Wiley & Sons, 2013.
(45) Wu, P.; Brand, L. Resonance Energy Transfer: Methods and Applications. *Anal Biochem* **1994**, *218* (1), 1–13. https://doi.org/10.1006/abio.1994.1134.
(46) Lucas, T.; Sarkar, M.; Atlas, Y.; Linger, C.; Renault, G.; Gazeau, F.; Gateau, J. Calibrated Photoacoustic Spectrometer Based on a Conventional Imaging System for in Vitro Characterization of Contrast Agents, 2022. https://hal.archives-ouvertes.fr/hal-02509232 (accessed 2022-07-27).
(47) Jaiswal, S.; Dutta, S. B.; Nayak, D.; Gupta, S. Effect of Doxorubicin on the Near-Infrared Optical Properties of Indocyanine Green. *ACS Omega* **2021**, *6* (50), 34842–34849. https://doi.org/10.1021/acsomega.1c05500.

(48) Zhou, E. Y.; Knox, H. J.; Liu, C.; Zhao, W.; Chan, J. A Conformationally Restricted Aza-BODIPY Platform for Stimulus-Responsive Probes with Enhanced Photoacoustic Properties. *J. Am. Chem. Soc.* **2019**, *141* (44), 17601–17609. https://doi.org/10.1021/jacs.9b06694.
(49) Grazon, C.; Rieger, J.; Charleux, B.; Clavier, G.; Méallet-Renault, R. Ultrabright BODIPY-Tagged Polystyrene Nanoparticles: Study of Concentration Effect on Photophysical Properties. *The Journal of Physical Chemistry C* **2014**, *118*, 13945–13952. https://doi.org/10.1021/jp502790w.
(50) Wagh, A.; Qian, S. Y.; Law, B. Development of Biocompatible Polymeric Nanoparticles for in Vivo NIR and FRET Imaging. *Bioconjug Chem* **2012**, *23* (5), 981–992. https://doi.org/10.1021/bc200637h.
(51) Andreiuk, B.; Reisch, A.; Bernhardt, E.; Klymchenko, A. Fighting Aggregation-Caused Quenching and Leakage of Dyes in Fluorescent Polymer Nanoparticles: Universal Role of Counterion. *Chemistry - An Asian Journal* **2019**, *14*. https://doi.org/10.1002/asia.201801592.
(52) Saxena, V.; Sadoqi, M.; Shao, J. Enhanced Photo-Stability, Thermal-Stability and Aqueous-Stability of Indocyanine Green in Polymeric Nanoparticulate Systems. *Journal of Photochemistry and Photobiology B: Biology* **2004**, *74* (1), 29–38. https://doi.org/10.1016/j.jphotobiol.2004.01.002.
(53) Reichardt, C. Solvatochromic Dyes as Solvent Polarity Indicators. *Chem. Rev.* **1994**, *94* (8), 2319–2358. https://doi.org/10.1021/cr00032a005.
(54) Galangau, O.; Dumas-Verdes, C.; Méallet-Renault, R.; Clavier, G. Rational Design of Visible and NIR Distyryl-BODIPY Dyes from a Novel Fluorinated Platform. *Org. Biomol. Chem.* **2010**, *8* (20), 4546–4553. https://doi.org/10.1039/C004812G.
(55) Hu, R.; Lager, E.; Aguilar-Aguilar, A.; Liu, J.; Lam, J. W. Y.; Sung, H. H. Y.; Williams, I. D.; Zhong, Y.; Wong, K. S.; Peña-Cabrera, E.; Tang, B. Z. Twisted Intramolecular Charge Transfer and Aggregation-Induced Emission of BODIPY Derivatives. *J. Phys. Chem. C* **2009**, *113* (36), 15845–15853. https://doi.org/10.1021/jp902962h.
(56) Wang, C.; Chi, W.; Qiao, Q.; Tan, D.; Xu, Z.; Liu, X. Twisted Intramolecular Charge Transfer (TICT) and Twists beyond TICT: From Mechanisms to Rational Designs of Bright and Sensitive Fluorophores. *Chem. Soc. Rev.* **2021**, *50* (22), 12656–12678. https://doi.org/10.1039/D1CS00239B.
(57) Kasha, M.; Rawls, H. R.; Ashraf El-Bayoumi, M. The Exciton Model in Molecular Spectroscopy. *Pure Appl. Chem.* **1965**, *11* (3), 371–392. https://doi.org/10.1351/pac196511030371.
(58) Würthner, F.; Kaiser, T. E.; Saha-Möller, C. R. J-Aggregates: From Serendipitous Discovery to Supramolecular Engineering of Functional Dye Materials. *Angew Chem Int Ed Engl* **2011**, *50* (15), 3376–3410. https://doi.org/10.1002/anie.201002307.
(59) Bünau, G. v. J. B. Birks: Photophysics of Aromatic Molecules. Wiley-Interscience, London 1970. 704 Seiten. Preis: 210s. **1970**. https://doi.org/10.1002/BBPC.19700741223.
(60) Gu, H.; Liu, W.; Zhen, S.; Long, S.; Sun, W.; Cao, J.; Zhao, X.; Du, J.; Fan, J.; Peng, X. "Internal and External Combined" Nonradiative Decay-Based Nanoagents for Photoacoustic Image-Guided Highly Efficient Photothermal Therapy. *ACS Appl. Mater. Interfaces* **2021**, *13* (39), 46353–46360. https://doi.org/10.1021/acsami.1c14020.
(61) Li, K.; Duan, X.; Jiang, Z.; Ding, D.; Chen, Y.; Zhang, G.-Q.; Liu, Z. J-Aggregates of Meso-[2.2]Paracyclophanyl-BODIPY Dye for NIR-II Imaging. *Nat Commun* **2021**, *12* (1), 2376. https://doi.org/10.1038/s41467-021-22686-z.
(62) Hu, W.; Miao, X.; Tao, H.; Baev, A.; Ren, C.; Fan, Q.; He, T.; Huang, W.; Prasad, P. N. Manipulating Nonradiative Decay Channel by Intermolecular Charge Transfer for Exceptionally Improved Photothermal Conversion. *ACS Nano* **2019**, *13* (10), 12006–12014. https://doi.org/10.1021/acsnano.9b06208.
(63) Lempke, L.; Fischer, T.; Bell, J.; Kraus, W.; Rurack, K.; Krause, N. Gold-Catalyzed Allene Cycloisomerization for Pyrrole Synthesis: Towards Highly Fluorinated BODIPY Dyes. *Org. Biomol. Chem.* **2015**, *13* (12), 3787–3791. https://doi.org/10.1039/C4OB02671C.
(64) Mula, S.; Ray, A. K.; Banerjee, M.; Chaudhuri, T.; Dasgupta, K.; Chattopadhyay, S. Design and Development of a New Pyrromethene Dye with Improved Photostability and Lasing Efficiency:

Theoretical Rationalization of Photophysical and Photochemical Properties. *J Org Chem* **2008**, *73* (6), 2146–2154. https://doi.org/10.1021/jo702346s.
(65) Duan, C.; Zhou, Y.; Shan, G.-G.; Chen, Y.; Zhao, W.; Yuan, D.; Zeng, L.; Huang, X.; Niu, G. Bright Solid-State Red-Emissive BODIPYs: Facile Synthesis and Their High-Contrast Mechanochromic Properties. *J. Mater. Chem. C* **2019**, *7* (12), 3471–3478. https://doi.org/10.1039/C8TC06421K.
(66) Descalzo, A.; Ashokkumar, P.; Shen, Z.; Rurack, K. On the Aggregation Behaviour and Spectroscopic Properties of Alkylated and Annelated Boron-Dipyrromethene (BODIPY) Dyes in Aqueous Solution. *ChemPhotoChem* **2019**, *4*. https://doi.org/10.1002/cptc.201900235.
(67) Tian, D.; Qi, F.; Ma, H.; Wang, X.; Pan, Y.; Chen, R.; Shen, Z.; Liu, Z.; Huang, L.; Huang, W. Domino-like Multi-Emissions across Red and near Infrared from Solid-State 2-/2,6-Aryl Substituted BODIPY Dyes. *Nat Commun* **2018**, *9* (1), 2688. https://doi.org/10.1038/s41467-018-05040-8.
(68) Hamon, C. L.; Dorsey, C. L.; Özel, T.; Barnes, E. M.; Hudnall, T. W.; Betancourt, T. Near-Infrared Fluorescent Aza-BODIPY Dye-Loaded Biodegradable Polymeric Nanoparticles for Optical Cancer Imaging. *J Nanopart Res* **2016**, *18* (7), 207. https://doi.org/10.1007/s11051-016-3518-7.
(69) Guo, X.; Li, M.; Wu, H.; Sheng, W.; Feng, Y.; Yu, C.; Jiao, L.; Hao, E. Near-IR Absorbing J-Aggregates of a Phenanthrene-Fused BODIPY as a Highly Efficient Photothermal Nanoagent. *Chem. Commun.* **2020**, *56* (93), 14709–14712. https://doi.org/10.1039/D0CC06014C.
(70) Zhang, Y.; Yuan, S.; Liu, P.; Jing, L.; Pan, H.; Ren, X.-K.; Chen, Z. J-Aggregation Induced Emission Enhancement of BODIPY Dyes via H-Bonding Directed Supramolecular Polymerization: The Importance of Substituents at Boron. *Org. Chem. Front.* **2021**, *8* (15), 4078–4085. https://doi.org/10.1039/D1QO00520K.
(71) Ozdemir, T.; Atilgan, S.; Kutuk, I.; Yildirim, L. T.; Tulek, A.; Bayindir, M.; Akkaya, E. U. Solid-State Emissive BODIPY Dyes with Bulky Substituents As Spacers. *Org. Lett.* **2009**, *11* (10), 2105–2107. https://doi.org/10.1021/ol9005568.
(72) Ho, L.-C.; Ou, C.-M.; Li, C.-L.; Chen, S.-Y.; Li, H.-W.; Chang, H.-T. Sensitive PH Probes of Retro-Self-Quenching Fluorescent Nanoparticles. *J. Mater. Chem. B* **2013**, *1* (18), 2425–2432. https://doi.org/10.1039/C3TB20146E.
(73) Wagh, A.; Jyoti, F.; Mallik, S.; Qian, S.; Leclerc, E.; Law, B. Polymeric Nanoparticles with Sequential and Multiple FRET Cascade Mechanisms for Multicolor and Multiplexed Imaging. *Small* **2013**, *9* (12), 2129–2139. https://doi.org/10.1002/smll.201202655.
(74) P. Green, A.; R. Buckley, A. Solid State Concentration Quenching of Organic Fluorophores in PMMA. *Physical Chemistry Chemical Physics* **2015**, *17* (2), 1435–1440. https://doi.org/10.1039/C4CP05244G.
(75) Ni, Y.; Kannadorai, R. K.; Yu, S. W.-K.; Chang, Y.-T.; Wu, J. Push–Pull Type Meso-Ester Substituted BODIPY near-Infrared Dyes as Contrast Agents for Photoacoustic Imaging. *Org. Biomol. Chem.* **2017**, *15* (21), 4531–4535. https://doi.org/10.1039/C7OB00965H.
(76) Hu, W.; Ma, H.; Hou, B.; Zhao, H.; Ji, Y.; Jiang, R.; Hu, X.; Lu, X.; Zhang, L.; Tang, Y.; Fan, Q.; Huang, W. Engineering Lysosome-Targeting BODIPY Nanoparticles for Photoacoustic Imaging and Photodynamic Therapy under Near-Infrared Light. *ACS Appl. Mater. Interfaces* **2016**, *8* (19), 12039–12047. https://doi.org/10.1021/acsami.6b02721.
(77) Laufer, J.; Jathoul, A.; Pule, M.; Beard, P. In Vitro Characterization of Genetically Expressed Absorbing Proteins Using Photoacoustic Spectroscopy. *Biomed Opt Express* **2013**, *4* (11), 2477–2490. https://doi.org/10.1364/BOE.4.002477.
(78) Miao, X.; Tao, H.; Hu, W.; Pan, Y.; Fan, Q.; Huang, W. Elucidating the Excited-State Dynamics Behavior in near-Infrared Bodipy Dye and Aggregates toward Biophotonics. *Sci. China Chem.* **2020**, *63* (8), 1075–1081. https://doi.org/10.1007/s11426-020-9731-0.
(79) Kulyk, B.; Taboukhat, S.; Akdas-Kilig, H.; Fillaut, J.-L.; Karpierz, M.; Sahraoui, B. Tuning the Nonlinear Optical Properties of BODIPYs by Functionalization with Dimethylaminostyryl Substituents. *Dyes and Pigments* **2017**, *137*, 507–511. https://doi.org/10.1016/j.dyepig.2016.10.045.

(80) Märk, J.; Schmitt, F.-J.; Theiss, C.; Dortay, H.; Friedrich, T.; Laufer, J. Photoacoustic Imaging of Fluorophores Using Pump-Probe Excitation. *Biomed. Opt. Express, BOE* **2015**, *6* (7), 2522–2535. https://doi.org/10.1364/BOE.6.002522.
(81) Paschotta, D. R. *Saturable Absorbers*. https://www.rp-photonics.com/saturable_absorbers.html (accessed 2022-04-28).

TOC Graphic